

Synchrosqueezed windowed linear canonical transform: A method for mode retrieval from multicomponent signals with crossing instantaneous frequencies

Shuixin Li^a, Jiecheng Chen^a, Qingtang Jiang^a, Jian Lu^b

^a*School of Mathematical Sciences, Zhejiang Normal University, Jinhua 321004, China*

^b*College of Mathematics and Statistics, Shenzhen University, Shenzhen 518060, China*

Abstract

In nature, signals often appear in the form of the superposition of multiple non-stationary signals. The overlap of signal components in the time-frequency domain poses a significant challenge for signal analysis. One approach to addressing this problem is to introduce an additional chirprate parameter and use the chirplet transform (CT) to elevate the two-dimensional time-frequency representation to a three-dimensional time-frequency-chirprate representation. From a certain point of view, the CT of a signal can be regarded as a windowed special linear canonical transform of that signal, undergoing a shift and a modulation.

In this paper, we develop this idea to propose a novel windowed linear canonical transform (WLCT), which provides a new time-frequency-chirprate representation. We discuss four types of WLCTs. In addition, we use a special X-ray transform to further sharpen the time-frequency-chirprate representation. Furthermore, we derive the corresponding three-dimensional synchrosqueezed transform, demonstrating that the WLCTs have great potential for three-dimensional signal separation.

Keywords: *windowed linear canonical transform; X-ray windowed linear canonical transform; synchrosqueezed windowed linear canonical transform; crossover instantaneous frequency; mode retrieval.*

Email addresses: lishuixin@zjnu.edu.cn (Shuixin Li), jcchen@zjnu.edu.cn (Jiecheng Chen), jiangq@zjnu.edu.cn (Qingtang Jiang), jianlu@szu.edu.cn (Jian Lu)

Nomenclature

Abbreviations

- CT – chirplet transform
- FrFT – fractional Fourier transform
- IF – instantaneous frequency
- LCT – linear canonical transform
- SSO – signal separation operator
- SST –synchrosqueezed transform
- SWLCT – synchrosqueezed windowed linear canonical transform
- SXWLCT – synchrosqueezed X-ray windowed linear canonical transform
- WFT – windowed Fourier transform
- WLCT – windowed linear canonical transform
- XWLCT – X-ray windowed linear canonical transform

Symbol Notations

- E_α – Rényi entropy based on the WLCT defined by (41) or (42)
- K – number of signal components
- M_k – the matrix of $M_k = [\phi_k''(t), 1; -1, 0]$
- $M_{\lambda,n}$ – parameter matrix of the WLCT
- N – the length of the signal
- N_c – the size of the chirprate bins
- N_f – the size of the frequency bins
- P_n – coefficient factor associated with $\mathcal{L}_g^{M_{\lambda,n}}(\tau)$ defined by (36)
- $\Lambda_x^{g,n}(t, \eta, \lambda)$ – chirprate reassignment operator defined by (37)
- $\mathcal{L}_x^M(u)$, $\mathcal{L}^M[x(\cdot)](u)$, $\mathcal{L}^M(x)(u)$ – LCT of $x(t)$ with matrix M
- $\mathcal{L}_g^{M_{\lambda,n}}(\tau)$ – WLCT of Gaussian function $g(t)$ with matrix $M_{\lambda,n}$
- $\Omega_x^{g,n}(t, \eta, \lambda)$ – frequency reassignment operator defined by (37)
- $S_x^{g,n}(t, \eta, \lambda)$ – SWLCT of $x(t)$ with matrix $M_{\lambda,n}$
- $S_x^{g,n}(t, \eta, \lambda)$ – SXWLCT of $x(t)$ with matrix $M_{\lambda,n}$
- $T_x^{g,n}(t, \eta, \lambda)$ – WLCT of $x(t)$ with matrix $M_{\lambda,n}$
- $\mathcal{T}_x^{g,n}(t, \eta, \lambda)$ – XWLCT of $x(t)$ with matrix $M_{\lambda,n}$
- $V_x^h(t, \eta)$ – WFT of $x(t)$ with window function h

1. Introduction

In real-world environments, signals often consist of multiple components. To accurately describe this, researchers use a simplified mathematical model represented as follows:

$$x(t) = \sum_{k=1}^K x_k(t) = \sum_{k=1}^K A_k(t)e^{2\pi i \phi_k(t)}, \quad (1)$$

where $A_k(t) > 0$ and $\phi'_k(t) > 0$ represent the instantaneous amplitude (IA) and instantaneous frequency (IF) of the k -th component, respectively. $A_k(t)$ is a slowly varying function of time. Each $x_k(t) = A_k(t)e^{2\pi i \phi_k(t)}$ represents a constituent component, or alternatively, a mode, of the signal $x(t)$ for $k = 1, 2, \dots, K$. One of the primary objectives in signal processing is the separation of individual modes $x_k(t)$ from a composite signal. This is pivotal for many applications and represents a fundamental challenge in the field.

Time-frequency analysis is an essential tool for characterizing the time-varying features and restoring the individual signal components of multicomponent non-stationary signals. Nevertheless, traditional linear time-frequency methods, such as the windowed Fourier transform (WFT), also known as the short time Fourier transform (STFT) [1] and the continuous wavelet transform [2, 3], are typically constrained by the uncertainty principle [4], making it difficult to achieve high time and frequency resolution simultaneously. Recently, Daubechies et al. developed a novel time-frequency analysis technique known as the synchrosqueezed transform (SST) [5]. Unlike the reassignment method (RM) [6], SST not only sharpens the time-frequency representation but also preserves invertibility. Since the publication of this method, subsequent research and extensions have led to a series of interesting and practical results. These include the 2nd-SST [7–9] and high-order SST [10], the synchroextracting transform (SET) [11], multiple-SST (MSST) [12], demodulation-based SST [13–16], time-reassigned SST [17–19], and second-order time-reassigned SST [20, 21], among others.

However, when the signal is composed of several components with crossover IF curves, most of the aforementioned methods fail to accurately reflect the signal characteristics in the regions near the intersection points. For example, consider a simple synthetic signal:

$$x(t) = e^{2\pi i(-4t^2+50t)} + e^{2\pi i(6t^2+10t)}, \quad t \in [0, 4], \quad (2)$$

sampled at 128 Hz. The IFs of the two components cross at $t = 2$ s and $\eta = 34$ Hz. Most time-frequency representations exhibit significant blurring around the intersection point, as illustrated in Fig. 1.

The chirplet transform (CT), proposed by Mann et al. [22], offers an effective solution to this issue by extending the two-dimensional time-frequency plane to a three-dimensional time-frequency-chirp space. For simplicity of presentation, we use “chirprate” to denote “chirp rate” in this paper.

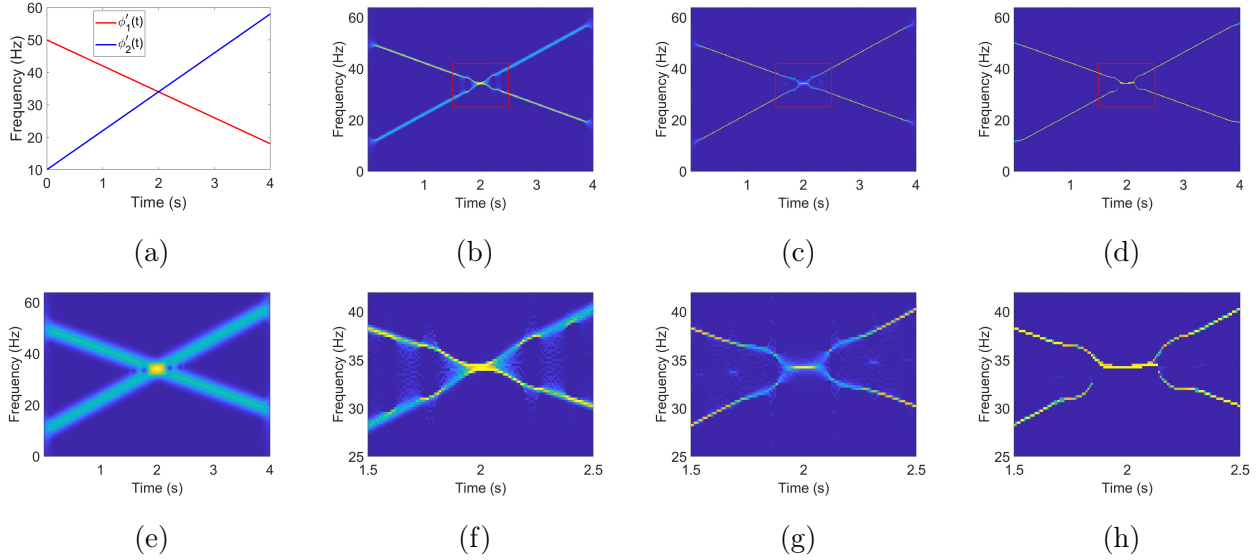


Figure 1: Time-frequency representations of $x(t)$. (a) IFs of signal; (b) SST; (c) 2nd SST; (d) MSST; (e) STFT; (f) SST (local zoom); (g) 2nd SST (local zoom); (h) MSST (local zoom).

In the time-frequency-chirprate space, under certain conditions, the components of non-stationary multicomponent signals can be well separated [23, 24]. Another transformation, known as the wavelet-chirplet transform (WCT), follows a similar concept. It also starts with the wavelet transform and elevates the time-scale plane to a three-dimensional time-scale-chirprate space [25].

The linear canonical transform (LCT) is a generalized integral transform that encompasses the Fourier transform and the fractional Fourier transform (FrFT) [26–28], serving as a fundamental tool in time-frequency analysis. It was independently introduced in the 1970s by Moshinsky, who formulated it within the framework of quantum mechanics [29], and by Collins, who derived it from optical system modeling [30]. Geometrically, the LCT corresponds to an affine transformation in the time-frequency plane. Over the past two decades, the combination of the LCT with traditional time-frequency analysis techniques has led to numerous innovative time-frequency analysis methods, such as the short time linear canonical transform [31, 32], the linear canonical wavelet transform [33, 34], the linear canonical Stockwell transform [35, 36], the Wigner-Ville distribution associated with LCT [37, 38], the spectrogram associated with the LCT [39]. These emerging methods have demonstrated unique strengths in handling non-stationary signals and have yielded a series of rich and meaningful research results.

In this paper, we propose a novel definition of the windowed linear canonical transform (WLCT), where the CT is a special case of the WLCT with a specific parameter matrix. Additionally, we introduce a new parameter through the LCT to elevate the time-frequency plane into a three-dimensional space, which we refer to as the time-frequency-chirprate space (when there is no ambiguity).

However, significant work remains to be done for accurately estimating the IFs and chirrate. The signal separation operator (SSO), was first introduced in [40] for multicomponent signal separation in the time-frequency plane. To recover the signal modes with crossing IFs, the SSO scheme was extended to the time-frequency-chirrate space in [41, 42]. Though the extended SSO scheme shows promise, its dependence on precise IF and chirrate estimations remains a limitation. Similar to the CT, the WLCT exhibits slow decay in the chirrate direction, which further complicates accurate chirrate extraction. To refine the estimations of IFs and chirrates, several methods based on the CT have been developed, including the synchrosqueezed CT [43, 44], the 3D extracting transform (TET) [45] and the multi-synchrosqueezed CT [46, 47].

In this paper, we propose three-dimensional synchrosqueezed transformations based on the WLCT scheme. Moreover, we introduce the composition of the X-ray transform and WLCT, termed X-ray WLCT (XWLCT) to significantly accelerate the decay rate in the chirrate direction. To achieve more accurate estimation of the IFs and chirrates, we further introduce synchrosqueezed transforms drawing upon the XWLCT. This approach yields promising results.

The remainder of this paper is organized as follows. Section 2 provides an overview of the definition and fundamental properties of the LCT. In Section 3, we introduce the windowed linear canonical transform (WLCT) and derive the associated mode retrieval formulas. The synchrosqueezed WLCT transform is developed in Section 4. Section 5 focuses on the XWLCT and its synchrosqueezed transform, and provides experimental validation. Implementation of the algorithms is described in Section 6. Finally, the paper concludes with a summary in Section 7.

2. Preliminary

2.1. Linear canonical transform (LCT)

In this paper, the Fourier transform of a signal $x(t)$ is defined as

$$\hat{x}(\xi) := \int_{\mathbb{R}} x(t) e^{-i2\pi\xi t} dt. \quad (3)$$

The LCT has been defined in numerous ways across various applications (e.g., [48, 49]). In this paper, we employ the definition presented in [49]. For simplicity, we denote the 2×2 parameter matrix $\begin{bmatrix} a & b \\ c & d \end{bmatrix}$ as $[a, b; c, d]$.

Definition 1. *Given a matrix $M = [a, b; c, d]$ with $a, b, c, d \in \mathbb{R}$ and $ad - bc = 1$, the LCT of a function $x(t)$ is defined as*

$$\mathcal{L}_x^M(u) := \begin{cases} \int_{\mathbb{R}} x(t) K_M(u, t) dt, & \text{if } b \neq 0; \\ \sqrt{d} e^{i\pi cdu^2} x(du), & \text{if } b = 0. \end{cases}$$

where the kernel function $K_M(u, t)$ is given by

$$K_M(u, t) := \frac{1}{\sqrt{bi}} e^{i\pi(\frac{a}{b}t^2 - \frac{2}{b}ut + \frac{d}{b}u^2)}.$$

Here, the expression $\frac{1}{\sqrt{bi}}$ is defined as

$$\frac{1}{\sqrt{bi}} = \frac{\exp(-i\frac{\pi}{4}\text{sign}(b))}{\sqrt{|b|}},$$

where $\text{sign}(b)$ denotes the sign of b , and $|b|$ is the absolute value of b . We use the notations $\mathcal{L}_x^M(u)$, $\mathcal{L}^M[x(\cdot)](u)$ and $\mathcal{L}^M(x)(u)$ to denote the LCT of the function $x(t)$ with respect to matrix M .

The matrix $M = [a, b; c, d]$, subject to the constraint $\det(M) = 1$, possesses three degrees of freedom, allowing for the variation of three independent parameters. This flexibility provides great convenience for analyzing signals.

2.2. Basic properties

In this subsection, we present selected fundamental mathematical properties of the LCT that are essential for subsequent analysis. For detailed proofs and a comprehensive enumeration, we refer the reader to [49].

Let $M = [a, b; c, d]$ with $\det(M) = 1$ be a parameter matrix.

1. Additivity:

$$\mathcal{L}^A \mathcal{L}^B[x(t)](u) = \mathcal{L}^{AB}[x(t)](u), \quad (4)$$

where A and B are matrices with determinant 1, and AB denotes their matrix product.

2. Differentiation Property: Suppose $y(t) = x'(t)$. Then,

$$\mathcal{L}_y^M(u) = 2\pi(aD_u - icu)\mathcal{L}_x^M(u), \quad (5)$$

where D_u denotes the differential operator with respect to u .

3. Generalized Parseval's Theorem:

$$\int_{\mathbb{R}} x(t)\overline{y(t)} dt = \int_{\mathbb{R}} \mathcal{L}_x^M(u)\overline{\mathcal{L}_y^M(u)} du, \quad (6)$$

where $\overline{y(t)}$ denotes the complex conjugate of $y(t)$.

3. Windowed linear canonical transform (WLCT): A new definition and properties

In this section, we propose a novel WLCT. We then conduct an in-depth study of its properties, focusing on its application in IF and chirprate estimations as well as mode retrieval. Our research targets multicomponent signals that exhibit crossover IFs. Notably, the WLCT we propose distinctly differs from the ones explored in the works [31, 32].

3.1. A new definition of WLCT

Before we introduce our WLCT, let us first recall the (modified) windowed Fourier transform (or short-time Fourier transform) of $x(t)$ using a window function $h(t)$, defined by

$$V_x^h(t, \eta) := \int_{\mathbb{R}} x(\tau) e^{-i2\pi\eta(\tau-t)} \overline{h(\tau-t)} d\tau = \int_{\mathbb{R}} x(t+\tau) e^{-i2\pi\eta\tau} \overline{h(\tau)} d\tau$$

By Parseval's theorem, we have

$$V_x^h(t, \eta) = \int_{\mathbb{R}} (x(t+\cdot) e^{-i2\pi\eta\cdot})^\wedge(\omega) \overline{\hat{h}(\omega)} d\omega.$$

Therefore, the windowed Fourier transform $V_x^h(t, \eta)$ of $x(t)$ is derived through the following sequence: A time shift of t units, $x(\tau) \rightarrow x(t+\tau)$; modulation by $e^{-i2\pi\eta\tau}$, $x(t+\tau) \rightarrow x(t+\tau) e^{-i2\pi\eta\tau}$; a Fourier transform with respect to τ , $(x(t+\tau) e^{-i2\pi\eta\tau})^\wedge(\omega)$; and averaging with a window function $g(\omega) = \overline{\hat{h}(\omega)}$.

Motivated by the above observation, we define the WLCT of $x(t)$ with a window function $g(t)$ as follows.

Definition 2. Given a parameter matrix $M = [a, b; c, d]$ with $\det(M) = 1$, we define the WLCT of $x(t)$ by

$$T_x^{g,M}(t, \eta) := \int_{\mathbb{R}} \mathcal{L}^{\widetilde{M}}(x(t+\cdot) e^{-i2\pi\eta\cdot})(u) g(u) du, \quad (7)$$

where for a parameter matrix $M = [a, b; c, d]$, \widetilde{M} denotes

$$\widetilde{M} := [d, b; c, a] = \begin{bmatrix} d & b \\ c & a \end{bmatrix}.$$

Note: In our definition of WLCT, we utilize \widetilde{M} rather than M on the right-hand side of (7) solely for the purpose of improving the clarity of the presentation that follows. The rationale for this substitution will be clarified shortly.

By (4) and (6), one has

$$\int_{\mathbb{R}} \mathcal{L}^{\widetilde{M}}([x(\cdot)])(u) \overline{y(u)} du = \int_{\mathbb{R}} x(\tau) \mathcal{L}^{\widetilde{M}^{-1}}[\overline{y(\cdot)}](\tau) d\tau = \int_{\mathbb{R}} x(\tau) \mathcal{L}^M[y(\cdot)](\tau) d\tau.$$

Hence, the $T_x^{g,M}(t, \eta)$ can be written as

$$T_x^{g,M}(t, \eta) := \int_{\mathbb{R}} x(t+\tau) e^{-i2\pi\eta\tau} \mathcal{L}^M(g)(\tau) d\tau. \quad (8)$$

Therefore, $T_x^{g,M}(t, \eta)$ can also be considered as a windowed Fourier transform of $x(t)$ with a window function $\mathcal{L}^M(g)$ obtained by the LCT of $g(t)$. Such window functions were also considered by Pei and Huang in the adaptive short-time Fourier transform [50], where they first applied the FrFT to a real Gaussian window function, obtaining a class of complex window functions termed chirp-modulated Gaussian functions. These chirp-modulated Gaussian functions significantly enhance energy concentration in time-frequency representations while maintaining invertibility [51].

3.2. Special WLCTs

The choice of the matrix M in the WLCT significantly impacts its properties and applications. Here, we explore the WLCTs with some special choices of M . We will consider the case where the window function $g(t)$ is the Gaussian function, defined by:

$$g(t) = e^{-\pi\alpha t^2}, \quad (9)$$

where $\alpha > 0$. To calculate $\mathcal{L}_g^M(u)$, the LCT of $g(t)$, we need the following formula (refer to formula (23) with $\nu = 0$ on p.121 of [52] or p.10 of [4])

$$\int_{\mathbb{R}} e^{-(\gamma+i\beta)t^2-i\omega t} dt = \frac{\sqrt{\pi}}{\sqrt{\gamma+i\beta}} e^{-\frac{\omega^2}{4(\gamma+i\beta)}}, \quad \gamma > 0, \quad (10)$$

where $\sqrt{\gamma+i\beta}$ denotes one of the square roots of the complex number $\gamma+i\beta$, with the condition that the real part of $\sqrt{\gamma+i\beta}$, denoted as $\text{Re}(\sqrt{\gamma+i\beta})$, is greater than zero.

By (10) and direct calculations, we have that $\mathcal{L}_g^M(u)$ is given by

$$\mathcal{L}_g^M(u) = \frac{1}{\sqrt{a+i\alpha b}} e^{-\pi \frac{\alpha - ibd\alpha^2 - iac}{b^2\alpha^2 + a^2} u^2} = Ce^{P\pi u^2}, \quad b \neq 0, \quad (11)$$

where

$$C = \frac{1}{\sqrt{a+i\alpha b}}, \quad P = \frac{id\alpha + c}{b\alpha - ia}. \quad (12)$$

When $b = 0$,

$$\mathcal{L}_g^M(u) = \sqrt{d} e^{-\pi\alpha d^2 u^2} e^{i\pi cdu^2},$$

which is a special case of (11) derived under the conditions $b = 0$ and $ad = 1$. Therefore, to encompass all scenarios without distinguishing whether b is zero or not, we can express $\mathcal{L}_g^M(u)$ in the unified form (11). Furthermore, we can derive the derivative of $\mathcal{L}_g^M(u)$,

$$D_u \mathcal{L}_g^M(u) = 2\pi P u \mathcal{L}_g^M(u). \quad (13)$$

Consider the analytic signal $x(t) = A(t)e^{i2\pi\phi(t)}$ under the regularity conditions

$$|A'(t)| \leq \epsilon_1, \quad |\phi'''(t)| \leq \epsilon_2, \quad (14)$$

where $\epsilon_1, \epsilon_2 > 0$ are sufficiently small. Then for a small time-localized interval of τ ,

$$x(t + \tau) \approx A(t)e^{i2\pi(\phi(t) + \phi'(t)\tau + \frac{\phi''(t)}{2}\tau^2)} = x(t)e^{i2\pi\phi'(t)\tau + i\pi\phi''(t)\tau^2}.$$

Thus, the WLCT of $x(t)$ can be expressed as

$$\begin{aligned} T_x^{g,M}(t, \eta) &\approx \int_{\mathbb{R}} x(t)e^{i2\pi(\phi'(t)-\eta)\tau + i\pi\phi''(t)\tau^2} \mathcal{L}_g^M(\tau) d\tau \\ &= \frac{1}{\sqrt{-i}} x(t) \mathcal{L}^{M_0}(\mathcal{L}^M(g))(\eta - \phi'(t)) = \frac{1}{\sqrt{-i}} x(t) \mathcal{L}_g^{M_0 M}(\eta - \phi'(t)), \end{aligned} \quad (15)$$

where the matrix $M_0 = [\phi''(t), 1; -1, 0]$, and the last equation follows the additivity property (4) of the LCT. With

$$M_0 M = \begin{bmatrix} \phi''(t) & 1 \\ -1 & 0 \end{bmatrix} \begin{bmatrix} a & b \\ c & d \end{bmatrix} = \begin{bmatrix} a\phi''(t) + c & b\phi''(t) + d \\ -a & -b \end{bmatrix}, \quad (16)$$

from (11), it follows that

$$T_x^{g,M}(t, \eta) \approx \frac{x(t)}{\sqrt{-i}} \frac{1}{\sqrt{a\phi''(t) + c + i\alpha(b\phi''(t) + d)}} e^{-\pi \frac{-\alpha b + i\alpha}{a\phi''(t) + c + i\alpha(b\phi''(t) + d)} (\eta - \phi'(t))^2}.$$

Hence

$$|T_x^{g,M}(t, \eta)| \approx A(t) L^{-\frac{1}{4}} e^{-\frac{\pi \alpha (\eta - \phi'(t))^2}{L}}, \quad (17)$$

where

$$L = (a\phi''(t) + c)^2 + \alpha^2(b\phi''(t) + d)^2.$$

It follows that the ridge of $|T_x^{g,M}(t, \eta)|$ along the frequency axis η provides an estimate of the IF $\phi'(t)$. In order to estimate the chirprate $\phi''(t)$, the key step is to investigate the minimization of L , as this process directly contributes to achieving an accurate estimation [24, 25].

Next, we examine the minimization of L by considering several specific choices of the matrix M . We introduce a parameter λ to represent the degree of freedom in selecting the matrix M .

I. Considering $M_{\lambda,1} = [\lambda, 1; -1, 0]$, the expression for L is

$$L_1(\lambda) = \alpha^2(\phi''(t))^2 + (\lambda\phi''(t) - 1)^2. \quad (18)$$

It becomes apparent that the minimization of $L_1(\lambda)$ occurs when $\lambda = 1/\phi''(t)$.

At this point,

$$\mathcal{L}^{M_{\lambda,1}}(g)(u) = \frac{1}{\sqrt{\alpha i + \lambda}} e^{-\frac{\pi \alpha u^2}{\lambda^2 + \alpha^2}} e^{-\frac{i\pi \lambda u^2}{\lambda^2 + \alpha^2}}. \quad (19)$$

II. With the matrix $M_{\lambda,2} = [1, 0; \lambda, 1]$, we derive the following for L :

$$L_2(\lambda) = \alpha^2 + (\phi''(t) + \lambda)^2. \quad (20)$$

Notably, $L_2(\lambda)$ achieves its minimum value under the condition $\lambda = -\phi''(t)$.

For this instance, the associated WLCT of $g(t)$ is

$$\mathcal{L}^{M_{\lambda,2}}(g)(u) = e^{-\pi \alpha u^2} e^{i\pi \lambda u^2}. \quad (21)$$

III. Given the matrix $M_{\lambda,3} = [1, -\lambda; 0, 1]$, the expression for L is defined as:

$$L_3(\lambda) = \alpha^2(-\lambda\phi''(t) + 1)^2 + (\phi''(t))^2.$$

Interestingly, the value of $L_3(\lambda)$ reaches its minimum when λ is set to $1/\phi''(t)$.

In this scenario,

$$\mathcal{L}^{M_{\lambda,3}}(g)(u) = \frac{1}{\sqrt{-\alpha\lambda i + 1}} e^{-\frac{\pi\alpha u^2}{\lambda^2\alpha^2+1}} e^{\frac{-i\pi\lambda\alpha^2 u^2}{\lambda^2\alpha^2+1}}. \quad (22)$$

IV. For the matrix $M_{\lambda,4} = [0, 1; -1, \lambda]$, the quantity L is given by:

$$L_4(\lambda) = \alpha^2(\phi''(t) + \lambda)^2 + 1.$$

It turns out that the minimum of $L_4(\lambda)$ is attained when λ equals $-\phi''(t)$.

Given this context,

$$\mathcal{L}^{M_{\lambda,4}}(g)(u) = \frac{1}{\sqrt{\alpha i}} e^{-\frac{\pi u^2}{\alpha}} e^{i\pi\lambda u^2}. \quad (23)$$

V. When $M_\theta = [\cos \theta, \sin \theta; -\sin \theta, \cos \theta]$, $\mathcal{L}^{M_\theta}(g)(u)$ corresponds to the FrFT of the Gaussian function g . To ensure that $\sin \theta$ is not zero, we choose θ within the interval $(0, \pi)$.

$$\begin{aligned} L_5 &= \alpha^2 (\sin \theta \phi''(t) + \cos \theta)^2 + (\cos \theta \phi''(t) - \sin \theta)^2 \\ &= \frac{\alpha^2}{1 + \cot^2 \theta} (\phi''(t) + \cot \theta)^2 + \frac{1}{1 + \cot^2 \theta} (\cot \theta \phi''(t) - 1)^2. \end{aligned}$$

Setting $\lambda = \cot \theta$, we write L_5 as :

$$L_5(\lambda) = \frac{\alpha^2}{1 + \lambda^2} (\phi''(t) + \lambda)^2 + \frac{1}{1 + \lambda^2} (\lambda \phi''(t) - 1)^2. \quad (24)$$

Taking the derivative of $L_5(\lambda)$ with respect to λ , we have

$$\begin{aligned} \frac{dL_5}{d\lambda} &= 2(1 - \alpha^2) \frac{(\lambda \phi''(t))^2 + \lambda^2 \phi''(t) - \lambda - \phi''(t)}{(1 + \lambda^2)^2} \\ &= 2(1 - \alpha^2) \frac{(\lambda \phi''(t) - 1)(\lambda + \phi''(t))}{(1 + \lambda^2)^2}. \end{aligned}$$

Therefore, the minimum value of $L_5(\lambda)$ can only be attained at the points where λ equals $1/\phi''(t)$, $-\phi''(t)$, or $\lambda \rightarrow \pm\infty$.

$$\begin{aligned} L_5(1/\phi''(t)) &= \alpha^2 \phi''(t)^2 + \alpha^2, \\ L_5(-\phi''(t)) &= \phi''(t)^2 + 1, \\ \lim_{\lambda \rightarrow \pm\infty} L_5(\lambda) &= \phi''(t)^2 + \alpha^2. \end{aligned}$$

It is clear that $L_5(\lambda)$ get its minimum value when

$$\lambda = \begin{cases} 1/\phi''(t), & \text{if } \alpha < 1; \\ -\phi''(t), & \text{if } \alpha > 1. \end{cases}$$

As we have observed from the above analysis, the two cases where $\alpha < 1$ and $\alpha > 1$ exhibit significant disparities. In order to clearly differentiate between these two scenarios and for the sake of more convenient presentation in the subsequent sections, we denote, although the quantities on the left-hand sides of the following two equations are identical:

$$\mathcal{L}^{M_{\lambda,5}}(g)(u) = \sqrt{\frac{-i - \lambda}{\alpha - i\lambda}} e^{-\frac{\alpha\pi u^2(1+\lambda^2)}{\alpha^2+\lambda^2}} e^{-\frac{i\pi u^2(1-\alpha^2)\lambda}{\alpha^2+\lambda^2}}, \quad \text{if } 0 < \alpha < 1, \quad (25)$$

$$\mathcal{L}^{M_{\lambda,6}}(g)(u) = \sqrt{\frac{-i - \lambda}{\alpha - i\lambda}} e^{-\frac{\alpha\pi u^2(1+\lambda^2)}{\alpha^2+\lambda^2}} e^{-\frac{i\pi u^2(1-\alpha^2)\lambda}{\alpha^2+\lambda^2}}, \quad \text{if } \alpha > 1. \quad (26)$$

Notably, the functions (19) and (22) exhibit a remarkable symmetry: Up to a constant $\sqrt{\alpha i}$, they are identical under the substitution $\alpha \leftrightarrow \frac{1}{\alpha}$. This symmetry is also observed between (21) and (23). Thus, the above first 4 cases can be reduced to the first 2 cases with

$$M_{\lambda,1} = [\lambda, 1; -1, 0], \quad M_{\lambda,2} = [1, 0; \lambda, 1].$$

To highlight the third variable λ , we write $T_x^{g,M_{\lambda,1}}(t, \eta)$ and $T_x^{g,M_{\lambda,2}}(t, \eta)$ as $T_x^{g,1}(t, \eta, \lambda)$ and $T_x^{g,2}(t, \eta, \lambda)$ respectively. In addition, write $T_x^{g,M_\theta}(t, \eta)$ as $T_x^{g,5}(t, \eta, \lambda)$ or $T_x^{g,6}(t, \eta, \lambda)$ depending on $\alpha < 1$ or $\alpha > 1$. More precisely,

$$T_x^{g,n}(t, \eta, \lambda) = \int_{\mathbb{R}} x(t + \tau) \mathcal{L}^{M_{\lambda,n}}(g)(\tau) e^{-2\pi i \eta \tau} d\tau, \quad \text{for } n = 1, 2, 5, 6, \quad (27)$$

where $\mathcal{L}^{M_{\lambda,1}}(g)(\tau)$ and $\mathcal{L}^{M_{\lambda,2}}(g)(\tau)$ are defined by (19) and (21) respectively, and $\mathcal{L}^{M_{\lambda,5}}(g)(\tau)$ and $\mathcal{L}^{M_{\lambda,6}}(g)(\tau)$ are defined by (25) and (26) respectively.

The chirplet transform (CT) [22] of $x(t)$ is defined by

$$C_x(t, \eta, \lambda) := \int_{\mathbb{R}} x(t + \tau) g(\tau) e^{-i2\pi \eta \tau} e^{-\pi i \lambda \tau^2} d\tau.$$

When $g(\tau)$ is the Gaussian function (9), CT is precisely the WLCT $T_x^{g,2}(t, \eta, -\lambda)$. Consequently, the CT is classified as a specific instance within the broader category of the WLCT.

3.3. Reconstruction Algorithm

For a multicomponent signal $x(t)$ given by (1), we assume that $x(t)$ satisfies the separation conditions:

$$|\phi'_k(t) - \phi'_j(t)| > 2\Delta_1 \quad \text{or} \quad |\phi''_k(t) - \phi''_j(t)| > 2\Delta_2, \quad t \in \mathbb{R}; \quad (28)$$

or alternatively,

$$|\phi'_k(t) - \phi'_j(t)| > 2\Delta'_1 \quad \text{or} \quad \frac{|\phi''_k(t) - \phi''_j(t)|}{|\phi''_k(t)| + |\phi''_j(t)|} > \Delta'_2, \quad t \in \mathbb{R}, \quad (29)$$

where Δ_1 , Δ_2 , Δ'_1 , and Δ'_2 are positive constants.

Remark 3.1. Condition (29) implies that the chirprate $\phi_k''(t)$ of each $x_k(t)$ must be nonzero. Consequently, we assume $\phi_k''(t) \neq 0$ for all signal components discussed henceforth in this paper. Additionally, for the purpose of comparing different types of WLCT $T_x^{g,n}(t, \eta, \lambda)$, we assume that the signals in this paper satisfy both conditions (28) and (29).

In [23], a group SSO reconstruction algorithm based on the CT was proposed to handle multi-component signals with crossover IF components. Initially, we assume that each signal component $x_k(t) = A_k(t)e^{2\pi i\phi_k(t)}$ satisfies condition (14). Under this assumption, $x_k(t)$ admits a local linear chirp approximation:

$$x_k(t + \tau) \approx x_k(t)e^{2\pi i\phi_k'(t)\tau + \pi i\phi_k''(t)\tau^2}.$$

Building on these concepts and analogous to (15), we obtain

$$T_x^{g,n}(t, \eta, \lambda) \approx \sum_{k=1}^K \frac{1}{\sqrt{-i}} x_k(t) \mathcal{L}_g^{M_k M_{\lambda,n}}(\eta - \phi_k'(t)). \quad (30)$$

where $M_k M_{\lambda,n}$ was defined in (16) by replacing M_0 with the matrix $M_k = [\phi_k''(t), 1; -1, 0]$ and M with $M_{\lambda,n}$ for $n = 1, 2, 5, 6$.

The synchrosqueezed WLCT (SWLCT, $S_x^n(t, \xi, \gamma)$) and synchrosqueezed X-ray WLCT (SXWLCT, $\mathcal{S}_x^n(t, \xi, \gamma)$) (both to be defined in subsequent sections) yield highly concentrated time-frequency-chirprate representations. The extracted ridge curves $\check{\xi}_k(t)$ and $\check{\gamma}_k(t)$, derived from either $S_x^n(t, \xi, \gamma)$ or $\mathcal{S}_x^n(t, \xi, \gamma)$, provide approximations of IFs and chirprates. This can be represented as:

$$\check{\xi}_k(t) \approx \phi_k'(t) \quad \text{and} \quad \check{\gamma}_k(t) \approx \phi_k''(t), \quad k = 1, 2, \dots, K.$$

Having established effective approximations for the IFs and chirprates, given the transform $T_x^{g,2}(t, \eta, \lambda)$ or $T_x^{g,6}(t, \eta, \lambda)$, we can reformulate (30) into a linear system of equations,

$$\begin{bmatrix} T_x^{g,n}(t, \check{\xi}_1(t), -\check{\gamma}_1(t)) \\ T_x^{g,n}(t, \check{\xi}_2(t), -\check{\gamma}_2(t)) \\ \vdots \\ T_x^{g,n}(t, \check{\xi}_K(t), -\check{\gamma}_K(t)) \end{bmatrix} = \begin{bmatrix} c_{1,1} & c_{1,2} & \cdots & c_{1,K} \\ c_{2,1} & c_{2,2} & \cdots & c_{2,K} \\ \vdots & \vdots & \ddots & \vdots \\ c_{K,1} & c_{K,2} & \cdots & c_{K,K} \end{bmatrix} \begin{bmatrix} x_1(t) \\ x_2(t) \\ \vdots \\ x_K(t) \end{bmatrix}.$$

By solving the linear system, the solution is given by

$$\begin{bmatrix} x_1(t) \\ x_2(t) \\ \vdots \\ x_K(t) \end{bmatrix} = \begin{bmatrix} c_{1,1} & c_{1,2} & \cdots & c_{1,K} \\ c_{2,1} & c_{2,2} & \cdots & c_{2,K} \\ \vdots & \vdots & \ddots & \vdots \\ c_{K,1} & c_{K,2} & \cdots & c_{K,K} \end{bmatrix}^{-1} \begin{bmatrix} T_x^{g,n}(t, \check{\xi}_1(t), -\check{\gamma}_1(t)) \\ T_x^{g,n}(t, \check{\xi}_2(t), -\check{\gamma}_2(t)) \\ \vdots \\ T_x^{g,n}(t, \check{\xi}_K(t), -\check{\gamma}_K(t)) \end{bmatrix}, \quad (31)$$

where for $n = 2$,

$$c_{i,j} = \frac{1}{\sqrt{\alpha - i(\check{\gamma}_j(t) - \check{\gamma}_i(t))}} e^{\frac{-\pi(\check{\xi}_i(t) - \check{\xi}_j(t))^2}{\alpha - i(\check{\gamma}_j(t) - \check{\gamma}_i(t))}}.$$

and for $n = 6$,

$$c_{i,j} = \frac{\sqrt{-i + \check{\gamma}_i(t)}}{\sqrt{\alpha + i\check{\gamma}_i(t)}} G_I^{-\frac{1}{2}} e^{\frac{\pi(\check{\xi}_i(t) - \check{\xi}_j(t))^2}{G_I}},$$

with $G_I = \frac{\alpha(1 + \check{\gamma}_i^2(t)) - i(1 - \alpha^2)\check{\gamma}_i(t)}{\alpha^2 + \check{\gamma}_i^2(t)} - i\check{\gamma}_j(t)$.

As for $\mathcal{L}^{M_{\lambda,1}}(g)(u)$ and $\mathcal{L}^{M_{\lambda,5}}(g)(u)$, drawing from similar ideas, we can derive an alternative reconstruction method.

$$\begin{bmatrix} x_1(t) \\ x_2(t) \\ \vdots \\ x_K(t) \end{bmatrix} = \begin{bmatrix} a_{1,1} & a_{1,2} & \cdots & a_{1,K} \\ a_{2,1} & a_{2,2} & \cdots & a_{2,K} \\ \vdots & \vdots & \ddots & \vdots \\ a_{K,1} & a_{K,2} & \cdots & a_{K,K} \end{bmatrix}^{-1} \begin{bmatrix} T_x^{g,n}(t, \check{\xi}_1(t), 1/\check{\gamma}_1(t)) \\ T_x^{g,n}(t, \check{\xi}_2(t), 1/\check{\gamma}_2(t)) \\ \vdots \\ T_x^{g,n}(t, \check{\xi}_K(t), 1/\check{\gamma}_K(t)) \end{bmatrix}, \quad (32)$$

where for $n = 1$,

$$a_{i,j} = \frac{1}{\sqrt{\alpha\check{\gamma}_j(t) + i(1 - \check{\gamma}_j(t)/\check{\gamma}_i(t))}} e^{\frac{-\pi(\alpha - i/\check{\gamma}_i(t))(\check{\xi}_i(t) - \check{\xi}_j(t))^2}{1 - \check{\gamma}_j(t)/\check{\gamma}_i(t) - i\alpha\check{\gamma}_j(t)}}.$$

and for $n = 5$,

$$a_{i,j} = \frac{\sqrt{-i + \check{\gamma}_i(t)}}{\sqrt{\alpha + i\check{\gamma}_i(t)}} G_{II}^{-\frac{1}{2}} e^{\frac{\pi(\check{\xi}_i(t) - \check{\xi}_j(t))^2}{G_{II}}},$$

with $G_{II} = \frac{\alpha(1 + 1/\check{\gamma}_i^2(t)) + i(1 - \alpha^2)/\check{\gamma}_i(t)}{\alpha^2 + 1/\check{\gamma}_i^2(t)} - i\check{\gamma}_j(t)$.

Note that when $C := [c_{\ell,k}]_{1 \leq \ell, k \leq K}$ is singular, C^{-1} in (31) means the pseudo-inverse of C . This also applies to $A := [a_{\ell,k}]_{1 \leq \ell, k \leq K}$ in (32). The modes of a signal can be retrieved by (31) or (32) once the IF and chirprate estimations $\check{\xi}_k(t)$ and $\check{\gamma}_k(t)$ are obtained. In the next two sections, we propose the SWLCT and SXWLCT to extract ridge curves $\check{\xi}_k(t)$ and $\check{\gamma}_k(t)$ as IF and chirprate estimations.

4. Synchrosqueezed windowed linear canonical transform (SWLCT)

Using the reassignment technique, the synchrosqueezed algorithm sharpens time-frequency representations. In [44], Chen and Wu proposed the synchrosqueezed chirplet transform (SCT), which

achieves high-resolution representation in the three-dimensional time-frequency-chirprate (TFC) space. As previously discussed, the CT is essentially a subset of the WLCT. This motivates the development of a synchrosqueezed algorithm for the entire WLCT framework.

First, we consider the signal $x(t)$ as a standard linear chirp signal, i.e., $x(t) = Ae^{2\pi i\phi(t)}$, where A is a positive constant and $\phi(t)$ is a quadratic function. Then

$$\begin{aligned} T_x^{g,n}(t, \eta, \lambda) &:= \int_{\mathbb{R}} x(t + \tau) e^{-i2\pi\eta\tau} \mathcal{L}^{M_{\lambda,n}}(g)(\tau) d\tau \\ &= \int_{\mathbb{R}} x(\tau) e^{-i2\pi\eta(\tau-t)} \mathcal{L}^{M_{\lambda,n}}(g)(\tau-t) d\tau \end{aligned} \quad (33)$$

$$= \int_{\mathbb{R}} A e^{2\pi i(\phi(t) + \phi'(t)\tau + \frac{1}{2}\phi''(t)\tau^2)} e^{-i2\pi\eta\tau} \mathcal{L}^{M_{\lambda,n}}(g)(\tau) d\tau. \quad (34)$$

Differentiating (34) with respect to t yields

$$\partial_t T_x^{g,n} = 2\pi i\phi'(t)T_x^{g,n} + 2\pi i\phi''(t)T_x^{\tau g,n}. \quad (35)$$

Here, $T_x^{\tau g,n}(t, \eta, \lambda)$ and $T_x^{\tau^2 g,n}(t, \eta, \lambda)$ denote the WLCT of $x(t)$ as defined in (27), with $\mathcal{L}^{M_{\lambda,n}}(g)(\tau)$ replaced by $\tau\mathcal{L}^{M_{\lambda,n}}(g)(\tau)$ and $\tau^2\mathcal{L}^{M_{\lambda,n}}(g)(\tau)$.

Under the condition $T_x^{g,n}(t, \eta, \lambda) \neq 0$, we can straightforwardly derive

$$\partial_t \left(\frac{\partial_t T_x^{g,n}}{T_x^{g,n}} \right) = 2\pi i\phi''(t) \left(1 + \partial_t \left(\frac{T_x^{\tau g,n}}{T_x^{g,n}} \right) \right).$$

Then, we define

$$\mu_x^{g,n}(t, \eta, \lambda) = \frac{\partial_t \left(\frac{\partial_t T_x^{g,n}}{T_x^{g,n}} \right)}{2\pi i \left(1 + \partial_t \left(\frac{T_x^{\tau g,n}}{T_x^{g,n}} \right) \right)}, \quad \omega_x^{g,n}(t, \eta, \lambda) = \frac{\partial_t T_x^{g,n} - 2\pi i\mu_x^{g,n}T_x^{\tau g,n}}{2\pi i T_x^{g,n}}.$$

Differentiating (33) directly yields

$$\partial_t T_x^{g,n} = 2\pi i\eta T_x^{g,n} - 2\pi P_n T_x^{\tau g,n},$$

where P_n denotes the value of P defined in (12) with corresponding matrices $M_{\lambda,n}$:

$$P_1 = -\frac{1}{\alpha - i\lambda}, \quad P_2 = i\lambda - \alpha, \quad P_5 = P_6 = \frac{i\lambda\alpha - 1}{\alpha - i\lambda}. \quad (36)$$

Similarly, we have

$$\partial_t T_x^{\tau g,n} = 2\pi i\eta T_x^{\tau g,n} - 2\pi P_n T_x^{\tau^2 g,n} - T_x^{g,n}.$$

These expressions yield

$$\mu_x^{g,n}(t, \eta, \lambda) = \frac{2\pi P_n (T_x^{g,n} T_x^{\tau^2 g,M} - T_f^{\tau g,n} T_f^{\tau g,n}) + (T_f^{g,n})^2}{2\pi i \left((T_x^{\tau g,n})^2 - T_f^{g,n} T_f^{\tau^2 g,n} \right)} = iP_n + \frac{(T_x^{g,n})^2}{2\pi i \left((T_x^{\tau g,n})^2 - T_x^{g,n} T_x^{\tau^2 g,n} \right)},$$

$$\omega_x^{g,n}(t, \eta, \lambda) = \eta + (iP_n - \mu_x^{g,n}) \frac{T_x^{\tau g,n}}{T_x^{g,n}} = \eta - \frac{T_x^{g,n} T_x^{\tau g,n}}{2\pi i \left((T_x^{\tau g,n})^2 - T_x^{g,n} T_x^{\tau^2 g,n} \right)}.$$

The frequency and chirprate reassignment operators are defined as

$$\Omega_x^{g,n}(t, \eta, \lambda) := \operatorname{Re}(\omega_x^{g,n}(t, \eta, \lambda)), \quad \Lambda_x^{g,n}(t, \eta, \lambda) := \operatorname{Re}(\mu_x^{g,n}(t, \eta, \lambda)). \quad (37)$$

where Re denotes the real part.

Definition 3. Let $T_x^{g,n}(t, \eta, \lambda), n = 1, 2, 5, 6$ be the WLCT of a signal $x(t)$ defined by (27). With the $\Omega_x^{g,n}(t, \eta, \lambda)$ and $\Lambda_x^{g,n}(t, \eta, \lambda)$ defined in (37), then we define the SWLCTs $S_x^n(t, \xi, \gamma)$ of $x(t)$ as follows:

For $n = 1, 5$,

$$S_x^n(t, \xi, \gamma) := \iint_{O_{t,n}} T_x^{g,n}(t, \eta, \lambda) \delta(\gamma - 1/\Lambda_x^{g,n}(t, \eta, \lambda)) \delta(\xi - \Omega_x^{g,n}(t, \eta, \lambda)) d\eta d\lambda; \quad (38)$$

and for $n = 2, 6$,

$$S_x^n(t, \xi, \gamma) := \iint_{O_{t,n}} T_x^{g,n}(t, \eta, \lambda) \delta(\gamma + \Lambda_x^{g,n}(t, \eta, \lambda)) \delta(\xi - \Omega_x^{g,n}(t, \eta, \lambda)) d\eta d\lambda, \quad (39)$$

where

$$O_{t,n} := \left\{ (\eta, \lambda) : T_x^{g,n}(t, \eta, \lambda) \neq 0, (T_x^{\tau g,n}(t, \eta, \lambda))^2 - T_x^{g,n}(t, \eta, \lambda) T_x^{\tau^2 g,n}(t, \eta, \lambda) \neq 0 \right\}. \quad (40)$$

To achieve effective SWLCTs, the parameter α must be carefully selected. An inappropriate selection of α may lead to an inaccurate representation in the time-frequency-chirprate domain. In practice, employing the Rényi entropy to determine the optimal value of α is an effective approach that has been widely utilized in previous studies, such as [10, 53].

The Rényi entropy based on the WLCT is defined as

$$E_\alpha := \frac{1}{1-\ell} \log_2 \frac{\iint_{\mathbb{R}^2} \int_0^\infty |T_x^{g_\alpha,n}(t, \eta, \lambda)|^{2\ell} \frac{d\lambda}{\lambda} dt d\eta}{\left(\iint_{\mathbb{R}^2} \int_0^\infty |T_x^{g_\alpha,n}(t, \eta, \lambda)|^2 \frac{d\lambda}{\lambda} dt d\eta \right)^\ell}, \quad \text{if } n = 1, 5, \quad (41)$$

or

$$E_\alpha := \frac{1}{1-\ell} \log_2 \frac{\iiint_{\mathbb{R}^3} |T_x^{g_\alpha,n}(t, \eta, \lambda)|^{2\ell} dt d\eta d\lambda}{\left(\iiint_{\mathbb{R}^3} |T_x^{g_\alpha,n}(t, \eta, \lambda)|^2 dt d\xi d\lambda \right)^\ell}, \quad \text{if } n = 2, 6, \quad (42)$$

where ℓ is a number greater than 2. In this paper, we let $\ell = 2.5$, a common value used in other studies [54]. A decrease in the Rényi entropy indicates increased concentration of the representation.

To identify the most concentrated representation, we seek the value of α that yields the lowest Rényi entropy, expressed as follows:

$$\alpha_{\text{opt}} := \underset{\alpha > 0}{\operatorname{argmin}} E_\alpha. \quad (43)$$

Once an appropriate value of α is determined, the synchrosqueezing algorithm is employed to obtain the refined time-frequency-chirprate representation $S_x^n(t, \xi, \gamma)$. The ridge curves $\xi_k(t)$ and $\gamma_k(t)$ are extracted from $S_x^n(t, \xi, \gamma)$ using a three-dimensional ridge extractor. This extractor identifies salient features in three-dimensional data through local maxima detection. For implementation details, see [46, 55]. Finally, the original signal can be reconstructed from the extracted ridge curves $\xi_k(t)$ and $\gamma_k(t)$ through the reconstruction algorithms given in (31) and (32).

Next we take the signal $x(t)$ given by (2) as an example to show the effectiveness of SWLCTs. The values of α obtained from (43) for $x(t)$ in (2) are $\alpha_1 = 0.050$, $\alpha_5 = 0.061$, $\alpha_2 = 6.2$ and $\alpha_6 = 23$, corresponding to $n = 1, 5, 2, 6$ respectively. In Fig. 2, we show IF estimation (the 1st column), chirprate (CR) estimation (the 2nd column), and (real part) errors of mode retrieval (3rd column) by SWLCTs.

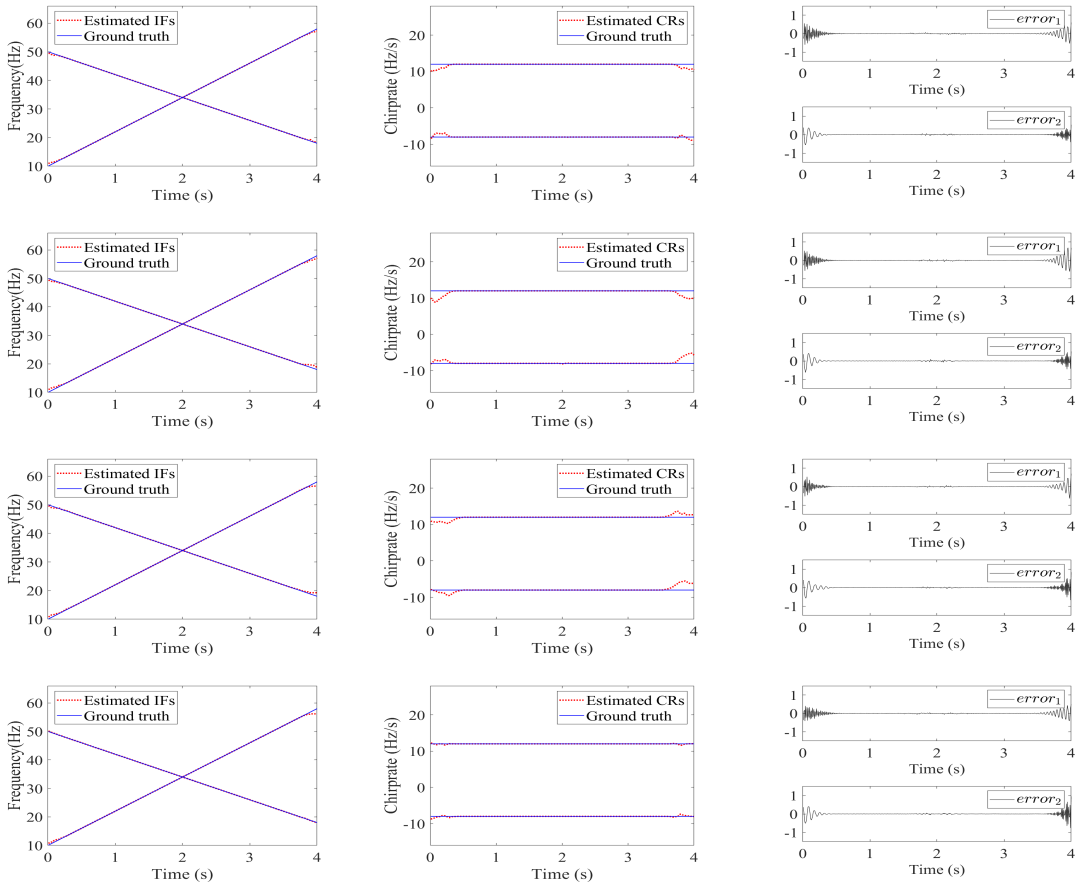


Figure 2: IF and chirprate estimations, and real part errors of mode retrieval: First row by $S_x^1(t, \xi, \gamma)$, Second row by $S_x^5(t, \xi, \gamma)$, Third row by $S_x^2(t, \xi, \gamma)$ and Fourth row by $S_x^6(t, \xi, \gamma)$.

To quantify the error of the retrieved mode, we employ the root mean square error (RMSE). Specifically, for a discrete signal $f = (f_1, f_2, \dots, f_N)$ and its estimation \tilde{f} (denoting the reconstructed signal), the RMSE is defined as $\text{error} = \frac{1}{\sqrt{N}} \|f - \tilde{f}\|_2$. To mitigate boundary effects, we calculate the error using the central portion of $f(t)$: $(f_{\lceil \frac{N}{8} \rceil}, f_{\lceil \frac{N}{8} \rceil+1}, \dots, f_{\lceil \frac{7N}{8} \rceil})$. The RMSEs are presented in Table 1, where error1 and error2 denote the RMSEs of two components of $x(t)$.

Table 1: RMSEs of mode retrieval for $x(t)$ in (2)

n	$n = 1$	$n = 5$	$n = 2$	$n = 6$
error1	0.0117	0.0113	0.0088	0.0118
error2	0.0102	0.0112	0.0091	0.0089

Overall, SWLCTs exhibit excellent performance in IF estimation, chirprate estimation, and mode retrieval. Notably, when $n = 6$, the $S_x^6(t, \xi, \gamma)$ yields the best chirprate estimation near the boundaries compared with the other three methods.

Next, let us look at the influence of the window parameter α on the accuracy of mode retrieval. Since the optimal α_n values determined by Rényi entropy differ significantly for different n , we take $n = 2$ as an example to illustrate the sensitivity of the reconstruction to variations in α . The α values are set to $6.2 + 0.1j$ for $j = -10, -9, \dots, 10$, while the optimal value $\alpha_2 = 6.2$ is obtained from (43) for $x(t)$ given by (2). With each of the parameters $\alpha = 6.2 + 0.1j$, we extract the IF and chirprate by $S_x^2(t, \xi, \gamma)$ and then reconstruct the signal components. Panel(a) of Fig. 3 shows the the reconstruction error of $x(t)$, which is defined as the sum of the RMSEs of the two components of $x(t)$. As shown in Panel(a) of Fig. 3, the SWLCT achieves high mode retrieval accuracy when α is within a reasonable range around α_2 . This trend generalizes to other types of WLCTs, as they also yield similar accuracy when α varies within a small region around their corresponding α_n .

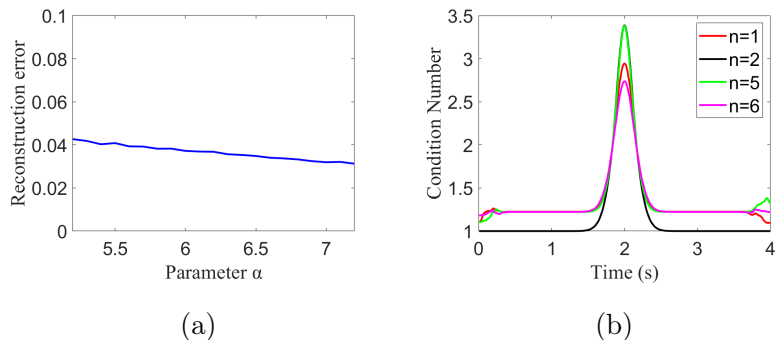


Figure 3: (a) reconstruction error with estimated IFs and chirprates; (b) condition numbers of inverse coefficient matrices.

As shown in (31) and (32), the reconstruction of the modes relies on the coefficient matrix C or A . The condition number of a matrix serves as an indicator of the sensitivity of a linear system's solution with respect to perturbations in the input data. For a non-singular square matrix M_0 , the condition number $\kappa(M_0)$ is given by

$$\kappa(M_0) := \|M_0\|_p \|M_0^{-1}\|_p, \quad (44)$$

where $\|M_0\|_p$ denotes the p -norm of the matrix M_0 and $\|M_0^{-1}\|_p$ denotes the p -norm of the inverse of M_0 . A singular or non-square matrix M can also have a condition number (see [56]). A high condition number indicates that the matrix is ill-conditioned, which can lead to numerical instability in solving linear systems.

For the signal $x(t)$ in (2), we present the condition numbers (with $p = 2$) of the coefficient matrices C and A in Panel(b) of Fig. 3. We can observe that the condition numbers are all relatively small, even near the crossing point of the two components. Specifically, at $t = 2$ s, the condition numbers for $n = 2$ and $n = 5$ are slightly larger than those for $n = 1$ and $n = 6$.

We take $n = 2$ as an example to show the sensitivity of the reconstruction to perturbations in IF and chirprate estimations. First, the individual IF and chirprate estimations are each perturbed by adding independent Gaussian white noise. For each estimation, the noise level is set to achieve a signal-to-noise ratio (SNR) of 15 dB with respect to its own power. The estimated ridges with small perturbations are shown in panels (a) and (b) of Fig. 4. Subsequently, via (31), we reconstruct the modes using the perturbed ridges and calculate the reconstruction errors. The reconstruction errors are shown in Panel(c) of Fig. 4. It can be seen that for small perturbations of IF and chirprate estimations, the reconstruction errors remain small; however, the errors near the crossing point are a little bit larger, which is consistent with the fact that the condition numbers are relatively large near the crossing point.

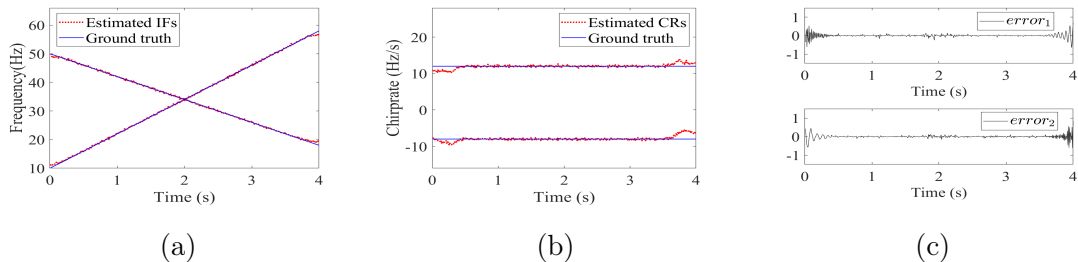


Figure 4: (a) IFs with small perturbations; (b) chirprates with small perturbations; (c) Reconstruction errors with small perturbations.

5. Synchrosqueezed X-ray windowed linear canonical transform (SXWLCT)

Though the SWLCTs can effectively separate the components of certain multicomponent signals, it may not be suitable for all scenarios. For instance, even when the signal components are linear chirp signals, the SWLCTs may not be able to accurately extract the IFs and chirprates.

Let

$$y(t) = y_1(t) + y_2(t), \quad y_1(t) = e^{i2\pi\phi_1(t)}, \quad y_2(t) = e^{i2\pi\phi_2(t)}, \quad (45)$$

where

$$\phi_1(t) = 4t^2 + 20t, \quad \phi_2(t) = 6t^2 + 12t.$$

The sampling frequency is 128 Hz and the time duration is $[0, 4)$ seconds. Note that the IFs crossover happens at time $t = 2$ s and frequency $\eta = 36$ Hz, and chirprates are 12 and 8 Hz/s respectively. These are all depicted in Fig. 5.

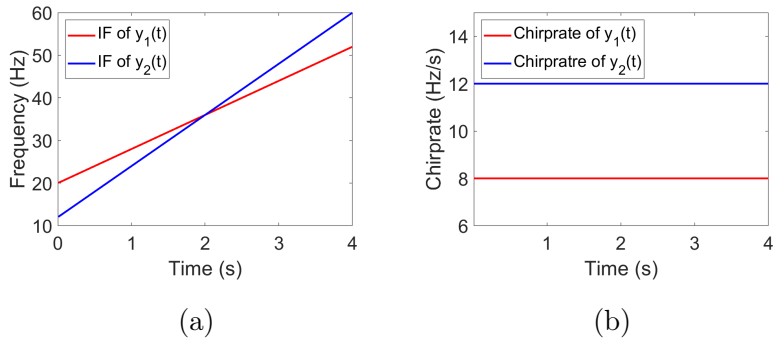


Figure 5: IFs and chirprates of y_1, y_2 . (a) IFs; (b) Chirprates.

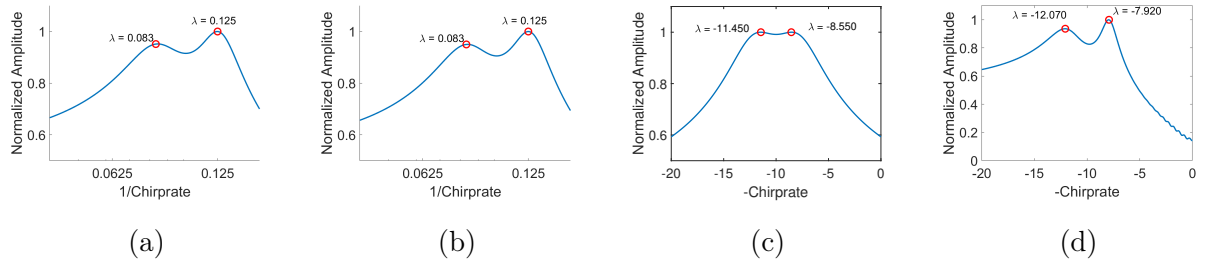


Figure 6: WLCTs of $y(t)$ at $t = 2$ s, $\eta = 36$ Hz. (a) $T_y^{g,1}(2, 36, \lambda)$; (b) $T_y^{g,5}(2, 36, \lambda)$; (c) $T_y^{g,2}(2, 36, \lambda)$; (d) $T_y^{g,6}(2, 36, \lambda)$.

Through (43), we obtain the α values as follows: For $\mathcal{L}^{M_{\lambda,1}}(g)(u)$ and $\mathcal{L}^{M_{\lambda,5}}(g)(u)$, α is 0.017 and 0.018, respectively; for $\mathcal{L}^{M_{\lambda,2}}(g)(u)$ and $\mathcal{L}^{M_{\lambda,6}}(g)(u)$, α is 2.5 and 80, respectively. We examine the slices of $|T_y^{g,n}(t, \eta, \lambda)|$ at the frequency intersection points in Fig. 6. From panels (a) and (b), distinct local maxima are evident around $\lambda = 0.125$ and $\lambda = 0.083$. In Panel(d), local maxima also

appear at $\lambda = -7.920$ and $\lambda = -12.070$, although the latter is less pronounced. Notably, in Panel(c), peaks are observed at $\lambda = -11.450$ and $\lambda = -8.550$, suggesting an obvious deviation from the ground truth.

The IFs and chirprates extracted from SWLCT are shown in Fig. 7. Near $t = 2$ s, $S_y^2(t, \eta, \lambda)$ and $S_y^6(t, \eta, \lambda)$ show minor errors in IF extraction and major errors in chirprate extraction. In contrast, $S_y^1(t, \eta, \lambda)$ and $S_y^5(t, \eta, \lambda)$ have negligible IF errors and more accurate chirprate extraction for high-chirprate components.

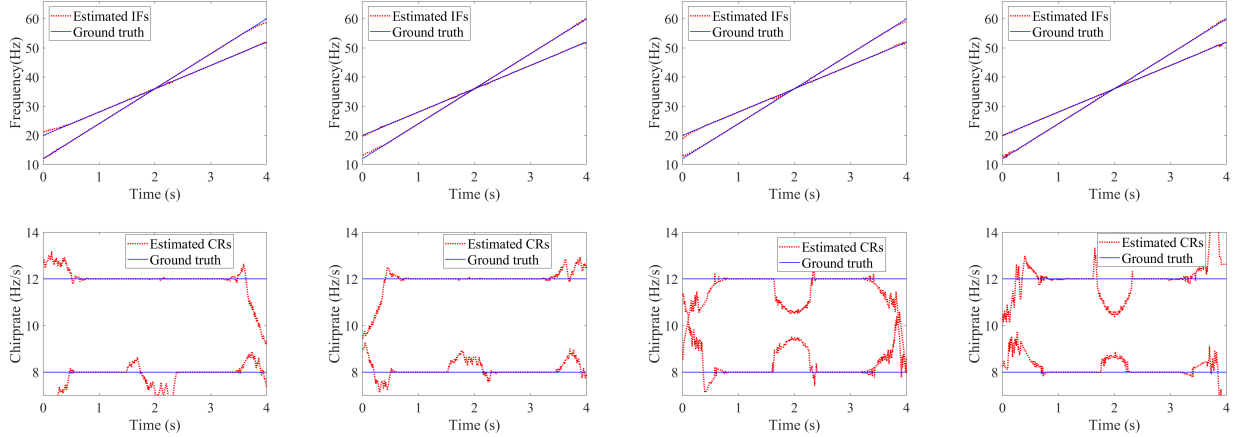


Figure 7: IF and chirprate estimations by SWLCT. First row shows IFs detected by: (1) $S_y^1(t, \xi, \gamma)$; (2) $S_y^5(t, \xi, \gamma)$; (3) $S_y^2(t, \xi, \gamma)$; (4) $S_y^6(t, \xi, \gamma)$. Second row shows corresponding chirprates detected by the same methods.

Referring to (17), the magnitude is given by

$$|T_x^{g,n}(t, \eta, \lambda)| = L_n(\lambda)^{-\frac{1}{4}} e^{-\frac{\pi \alpha(\eta - \phi'(t))^2}{L_n(\lambda)}}, \quad (46)$$

where $L_n(\lambda)$ is defined by (18) for $n = 1$, (20) for $n = 2$, (24) for $n = 5$ or $n = 6$. When the frequency η is fixed near $\phi'(t)$, the decay of $|T_y^{g,n}(t, \eta, \lambda)|$ with respect to λ is determined by the term $L_n(\lambda)^{-\frac{1}{4}}$. This slow decay gives rise to large errors in chirprate estimation. To achieve a faster decay rate in the chirprate direction, we propose the X-ray WLCT (XWLCT). The X-ray wavelet-chirplet transform was introduced in [57] to obtain a sharper time-scale-chirprate representation of a signal.

The continuous X-ray transform of a 3D function $f(z_1, z_2, z_3)$, where $(z_1, z_2, z_3) \in \mathbb{R}^3$, is denoted by Pf . It encompasses the collection of all line integrals of f [58]. More precisely, the X-ray transform of f along a given line s parameterized as $s(v) = z + v\theta, v \in \mathbb{R}$, is defined by

$$Pf(z, \theta) := \int_{-\infty}^{\infty} f(z + v\theta) dv.$$

Consider a window function $h(v)$ such that $\int_{-\infty}^{\infty} h(v) dv = 1$. We can then define a localized X-ray

transform of f as:

$$\mathcal{P}f(z, \theta) := \int_{-\infty}^{\infty} f(z + v\theta)h(v)dv.$$

This localized variant integrates the function along the line, but critically, it weights the contribution of each point on the line by the window function $h(v)$. This localization proves beneficial in diverse applications by concentrating the transform on a specific segment of the line.

Definition 4. Let $T_x^{g,n}(t, \eta, \lambda)$ be the WLCTs of $x(t)$, as defined in definition (27), and $h(v)$ be a nonnegative window function that satisfies $\int_{-\infty}^{\infty} h(v)dv = 1$.

1. When $n = 1$ or 5 , the XWLCT of $x(t)$ is defined as

$$\mathcal{T}_x^{g,n}(t, \eta, \lambda) := \int_{-\infty}^{\infty} |T_x^{g,n}(t + v, \eta + \frac{v}{\lambda}, \lambda)|h(v)dv, \quad (47)$$

2. When $n = 2$ or 6 , the XWLCT of $x(t)$ is given by

$$\mathcal{T}_x^{g,n}(t, \eta, \lambda) := \int_{-\infty}^{\infty} |T_x^{g,n}(t + v, \eta - \lambda v, \lambda)|h(v)dv. \quad (48)$$

In the definitions presented in (47) and (48), the transformations can be interpreted as a (localized) X-ray transform of $|T_x^{g,n}(t, \eta, \lambda)|$ along the (un-normalized) direction vector $\beta = (1, \frac{1}{\lambda}, 0)$ for (47) and $\beta = (1, -\lambda, 0)$ for (48) respectively. This characteristic is the reason why such transformations are termed as X-ray transforms.

Next we explain why $\mathcal{T}_x^{g,n}(t, \eta, \lambda)$ exhibits a faster decay rate than $T_x^{g,n}(t, \xi, \lambda)$ in the λ direction.

When time t is incremented by a small interval v , we have

$$\phi'(t + v) \approx \phi'(t) + \phi''(t)v, \quad \phi''(t + v) \approx \phi''(t). \quad (49)$$

Given the signal $x(t) = Ae^{i2\pi\phi(t)}$, from (46) and (49), when t move to $t + v$, then $L_n(\lambda)$ remains essentially unchanged. Thus, our focus shifts to the factor $(\eta - \phi'(t))^2$ in the exponent of e . Under the condition (49), the factor $(\eta - \phi'(t))^2$ in the XWLCTs assumes two distinct approximate expressions:

$$(\eta + \frac{v}{\lambda} - \phi'(t + v))^2 \approx (\eta - \phi'(t) + \frac{v}{\lambda}(1 - \lambda\phi''(t)))^2,$$

or

$$(\eta - \lambda v - \phi'(t + v))^2 \approx (\eta - \phi'(t) - v(\lambda + \phi''(t)))^2.$$

Thus, for $n = 1, 5$, we have:

$$\mathcal{T}_x^{g,n}(t, \eta, \lambda) = \left| T_x^{g,n}(t + v, \eta + \frac{v}{\lambda}, \lambda) \right| \approx L_n^{-\frac{1}{4}} e^{-\frac{\pi\alpha(\eta - \phi'(t) + \frac{v}{\lambda}(1 - \lambda\phi''(t)))^2}{L_n}}, \quad (50)$$

and for $n = 2, 6$,

$$\mathcal{T}_x^{g,n}(t, \eta, \lambda) = |T_x^{g,n}(t + v, \eta - \lambda v, \lambda)| \approx L_n^{-\frac{1}{4}} e^{-\frac{\pi \alpha(\eta - \phi'(t) - v(\lambda + \phi''(t)))^2}{L_n}}. \quad (51)$$

Both (50) and (51) show that a larger v leads to faster decay of the XWLCTs magnitude with respect to λ . However, a good approximation requires a small v (see (49)). To address this contradiction, we use a local integration with a window function $h(v)$ in (47) and (48).

To illustrate the capability of the XWLCTs, we present the slice of $\mathcal{T}_y^{g,n}(t, \eta, \lambda)$ at the intersection point in Fig. 8. As shown in panels (c) and (d) of Fig. 8, two distinct peaks are clearly observed when λ is set to -12 and -8 , whereas panels (a) and (b) show the peaks occur at $\lambda = 0.125$ and $\lambda = 0.083$ respectively. By comparing with Fig. 6, it can be observed that the XWLCTs $\mathcal{T}_y^{g,n}(t, \eta, \lambda)$ significantly increase the decay rate in the λ direction, thereby forming a more concentrated time-frequency-chirprate representation.

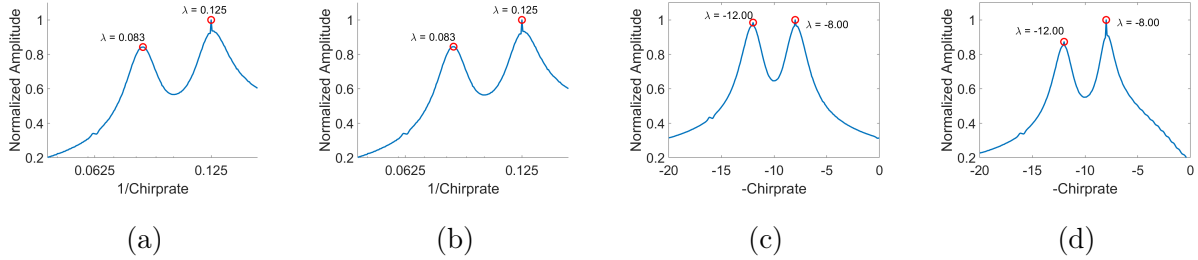


Figure 8: XWLCTs of $y(t)$ at $t = 2$ s, $\eta = 36$ Hz. (a) $\mathcal{T}_y^{g,1}(2, 36, \lambda)$; (b) $\mathcal{T}_y^{g,5}(2, 36, \lambda)$; (c) $\mathcal{T}_y^{g,2}(2, 36, \lambda)$; (d) $\mathcal{T}_y^{g,6}(2, 36, \lambda)$.

To further enhance the XWLCTs, we introduce the synchrosqueezed XWLCTs (SXWLCTs) based on the XWLCTs.

Definition 5. Let $\mathcal{T}_x^{g,n}(t, \eta, \lambda)$ be the XWLCTs of a signal $x(t)$ defined by (47) or (48). The SXWLCTs of $x(t)$ are defined as follows:

$$\text{For } n = 1, 5, \quad \mathcal{S}_x^n(t, \xi, \gamma) := \iint_{O_{t,n}} \mathcal{T}_x^{g,n}(t, \eta, \lambda) \delta(\gamma - 1/\Lambda_x^{g,n}(t, \eta, \lambda)) \delta(\xi - \Omega_x^{g,n}(t, \eta, \lambda)) d\eta d\lambda; \quad (52)$$

$$\text{and for } n = 2, 6, \quad \mathcal{S}_x^n(t, \xi, \gamma) := \iint_{O_{t,n}} \mathcal{T}_x^{g,n}(t, \eta, \lambda) \delta(\gamma + \Lambda_x^{g,n}(t, \eta, \lambda)) \delta(\xi - \Omega_x^{g,n}(t, \eta, \lambda)) d\eta d\lambda, \quad (53)$$

where $\Omega_x^{g,n}(t, \eta, \lambda)$, $\Lambda_x^{g,n}(t, \eta, \lambda)$, and $O_{t,n}$ are defined by (37) and (40) respectively.

The results of the IF estimations (first column), chirprate estimations (second column), and the real-part errors of mode retrieval (third column) obtained via SXWLCTs are presented in Fig. 9.

Compared with SWLCTs (see Fig. 7), the SXWLCTs show higher accuracy in both IF and chirprate estimation, with improved mode retrieval capability. Notably, in the mode retrieval process, the $\mathcal{S}_x^1(t, \xi, \gamma)$, $\mathcal{S}_x^5(t, \xi, \gamma)$, and $\mathcal{S}_x^6(t, \xi, \gamma)$ exhibit significantly smaller errors when recovering high-chirprate components.

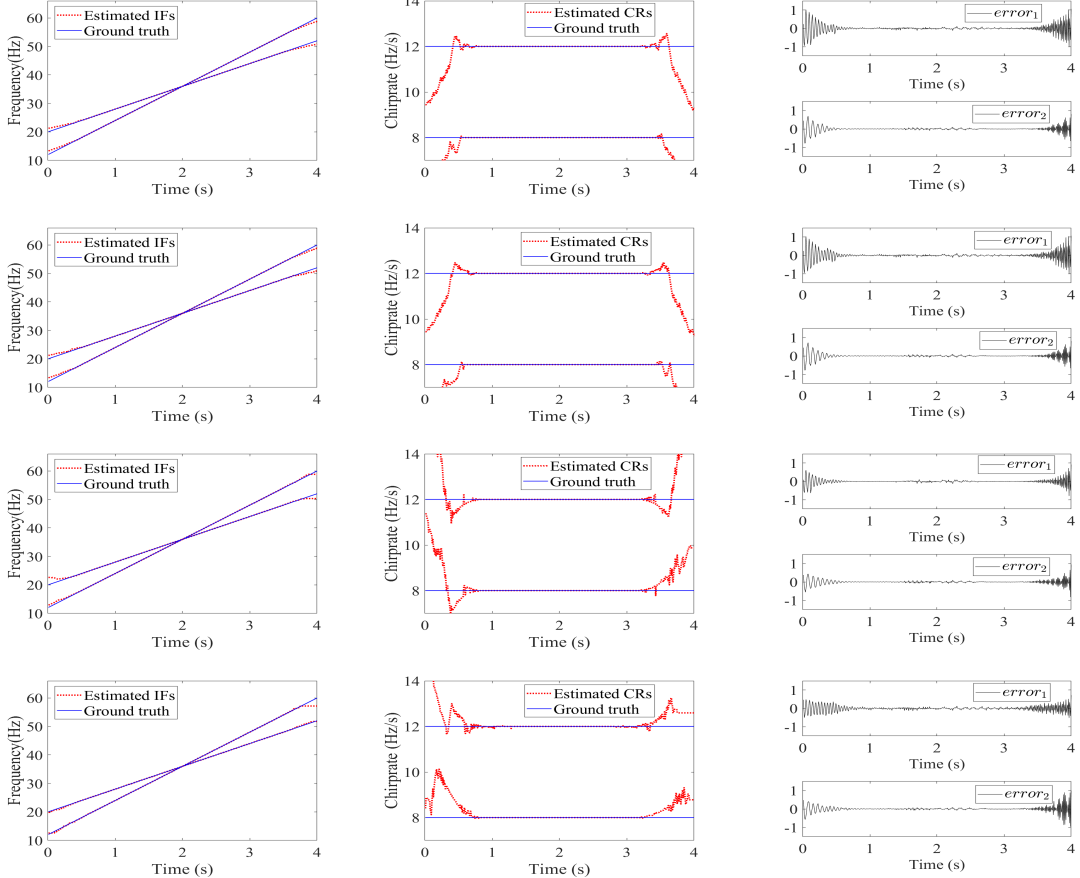


Figure 9: IF and chirprate estimations, and real part errors of mode retrieval by SXWLCT. First row by $\mathcal{S}_y^1(t, \xi, \gamma)$, Second row by $\mathcal{S}_y^5(t, \xi, \gamma)$, Third row by $\mathcal{S}_y^2(t, \xi, \gamma)$ and Fourth row by $\mathcal{S}_y^6(t, \xi, \gamma)$.

Furthermore, for a more intuitive understanding, we present the three-dimensional distributions of the WLCTs and XWLCTs in Fig. 10. The XWLCT is designed to enhance concentration specifically along the chirprate dimension by accelerating its decay, thereby isolating the signal from cross-component interference. This refined representation in the chirprate domain is the key factor that allows the SXWLCTs to provide more accurate estimations of both the chirprate and the IF than the SWLCTs.

For a comparative analysis, Fig. 11 presents the results obtained by the TET [45] and MESCT [46] methods for the signal in (45). Visually, the TET and MESCT exhibit significant deviations in estimating the IFs and chirprates, which leads to considerable errors in the subsequent mode retrieval.

The performance is evaluated using the RMSE of the retrieved modes, as summarized in Table 2. The consistently lower RMSE values of our method confirm its superior capability in processing such signals.

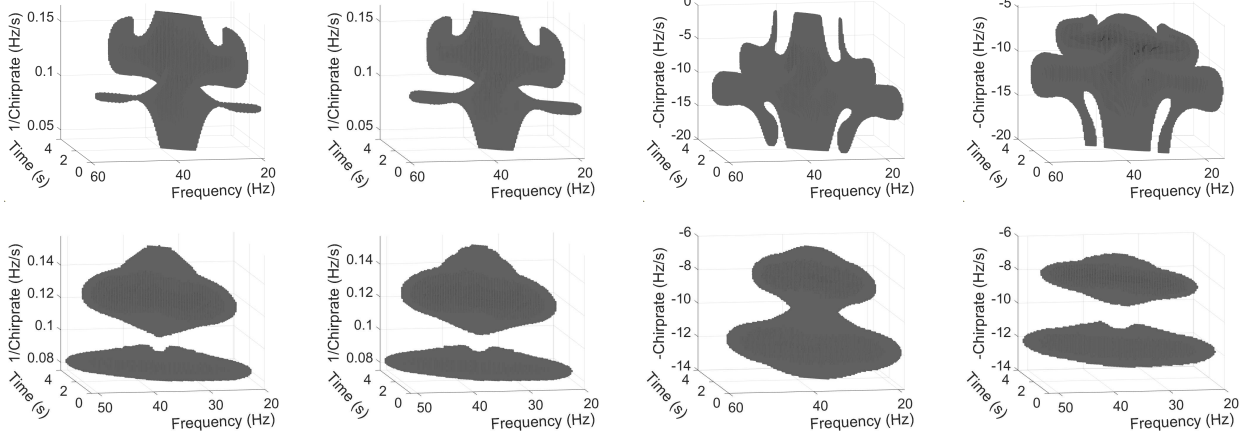


Figure 10: Three-dimensional representations of the WLCTs and XWLCTs. First row (left to right): WLCTs with $n = 1, 5, 2, 6$; Second row: Corresponding XWLCTs.

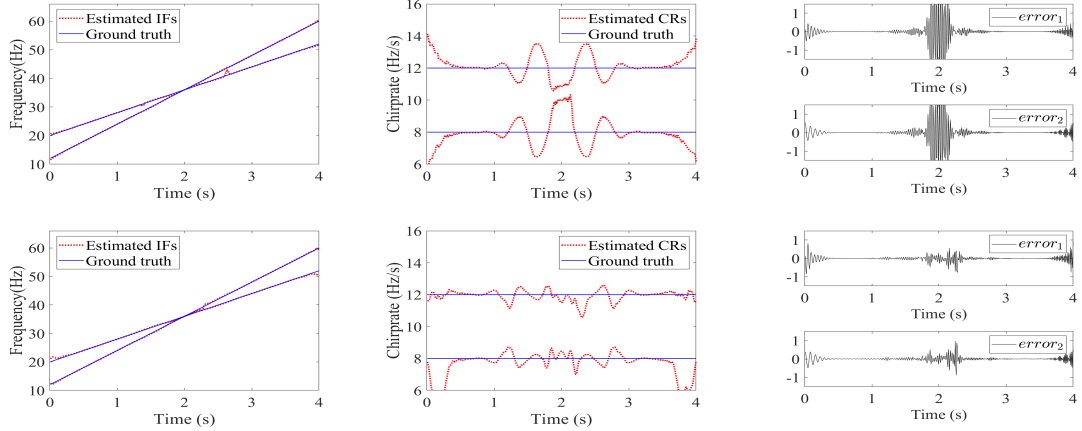


Figure 11: IF and chirrate estimations, along with real part errors of mode retrieval using TET and MESCT. First row: Results from TET. Second row: Results from MESCT (with three squeezes).

Table 2: RMSEs of mode retrieval for $y(t)$ in (45)

$\mathcal{S}_y^n(t, \xi, \gamma)$	$n = 1$	$n = 5$	$n = 2$	$n = 6$	TET	MESCT
error1	0.0359	0.0256	0.0376	0.0585	0.5785	0.0812
error2	0.0225	0.0253	0.0215	0.0273	0.5725	0.0788

Next, we consider

$$z(t) = z_1(t) + z_2(t), \quad z_1(t) = e^{i2\pi\phi_1(t)}, \quad z_2(t) = e^{i2\pi\phi_2(t)}, \quad t \in [0, 8], \quad (54)$$

where $\phi_1(t) = 2t^2 + 18t$ and $\phi_2(t) = 2t^2 + 18t + \frac{64}{\pi} \cos(\frac{\pi t}{8} + \frac{\pi}{2})$. The sampling frequency is 128 Hz and corresponding window parameters are 0.062, 0.06, 1, and 29 for $n = 1, 5, 2, 6$. The IFs are expressed as $\phi'_1(t) = 4t + 18$ and $\phi'_2(t) = 4t + 18 - 8 \sin(\frac{\pi t}{8} + \frac{\pi}{2})$, respectively, and they intersect at the point $t = 4$ s, $\eta = 34$ Hz. The chirprates of the two modes are defined as $\phi''_1(t) = 4$ and $\phi''_2(t) = 4 - \pi \cos(\frac{\pi t}{8} + \frac{\pi}{2})$. The IFs and chirprates of $z_1(t), z_2(t)$ are shown in Fig. 12.

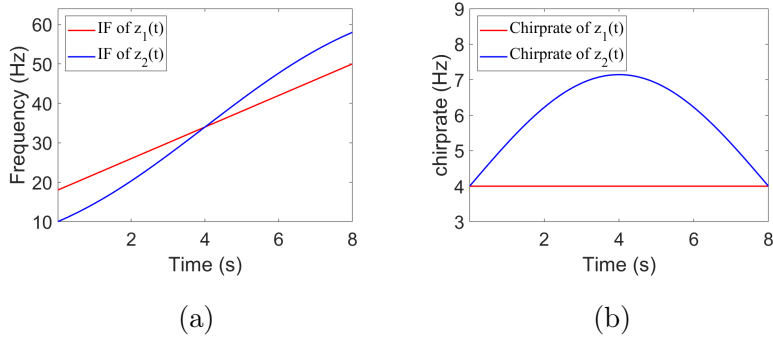


Figure 12: IFs and chirprates of z_1, z_2 . (a) IFs; (b) Chirprates.

For the signal $z(t)$, the SXWLCT methods also demonstrate their capability to separate signal modes and accurately extract the IFs, as shown in Fig. 13. However, slight deviations occur in the estimated chirprate near the intersection points of the sinusoidal components. Despite this, the SXWLCTs achieve good mode retrieval. Notably, when using $\mathcal{S}_x^1(t, \xi, \gamma)$ and $\mathcal{S}_x^5(t, \xi, \gamma)$ to recover modes, the recovered high-chirprate components exhibit smaller errors compared to the other modes.

At the end of this section, we apply the SWLCTs to a real-world signal to demonstrate its effectiveness in time-frequency analysis. The acoustic data used in this experiment are from killer whale group communications [55, 59], which provide valuable insights into marine animal behavior. Such signals are challenging to analyze due to the diversity of vocal repertoires and strong background noise in the underwater environment. The original data were downsampled to a rate of 7500 Hz. Fig. 14 shows two crossing IF curves between 1900-2400 Hz during the 1.6-2 s interval, which is highlighted by a red rectangle in Panel(a) of STFT with an enlarged part presented in Panel(b).

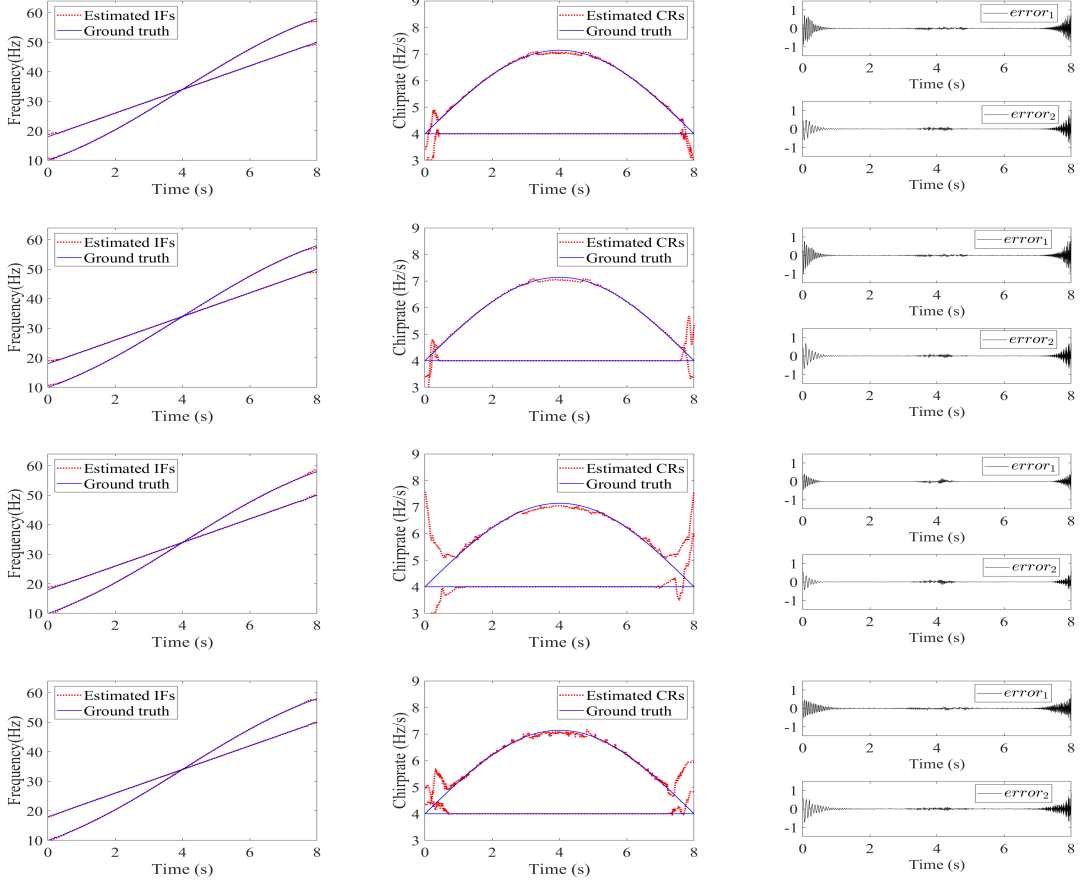


Figure 13: IFs and chirprates estimations, and real part errors of mode retrieval by SXWLCT. First row by $\mathcal{S}_z^1(t, \xi, \gamma)$, Second row by $\mathcal{S}_z^5(t, \xi, \gamma)$, Third row by $\mathcal{S}_z^2(t, \xi, \gamma)$ and Fourth row by $\mathcal{S}_z^6(t, \xi, \gamma)$.

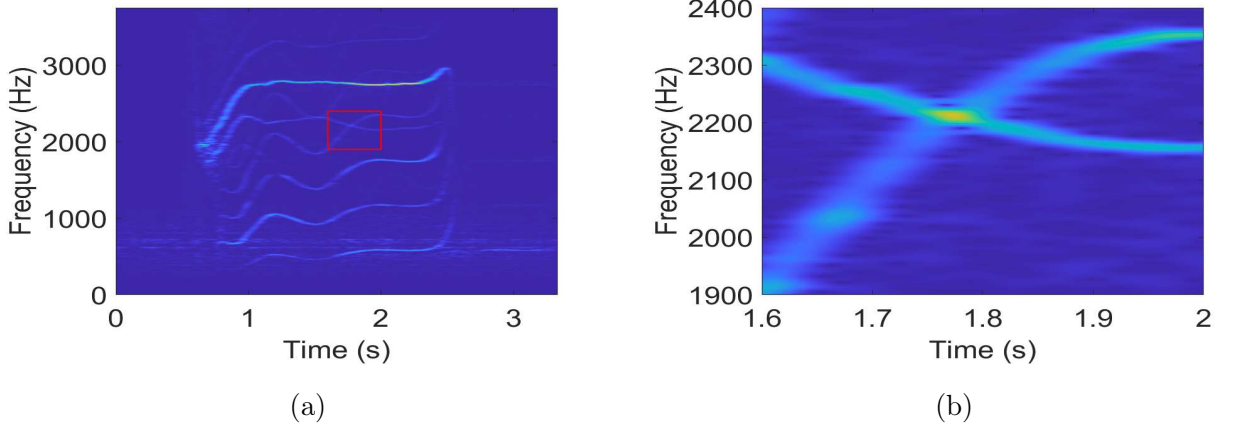


Figure 14: (a) STFT of killer whale acoustic data; (b) Enlarged part with crossover IFs.

To enable an intuitive assessment, we provide three-dimensional representations of both the WLCT and its X-ray transform, using $n = 6$ as a representative example (see Fig. 15). The analysis,

conducted over the time interval of 1.6–2 s and the frequency range of 1900–2400 Hz, clearly illustrates the enhanced energy concentration of the XWLCTs along the chirrate dimension. This concentrated representation consequently leads to sharper time-frequency ridges, which are subsequently extracted using the SXWLCTs within the same region.

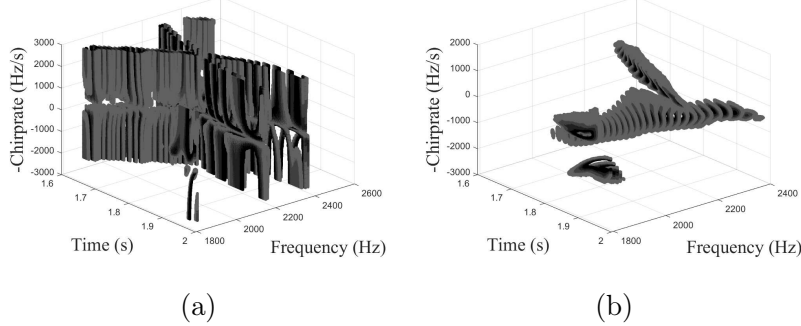


Figure 15: (a) WLCT with $n = 2$; (b) XWLCT with $n = 2$.

For a comparative analysis, the TET and MESCT methods are also employed to extract the IF ridges. As evidenced by Fig. 16, the proposed SXWLCTs provide accurate IF estimations, whereas significant deviations are observed in both TET and MESCT, especially near intersection points.

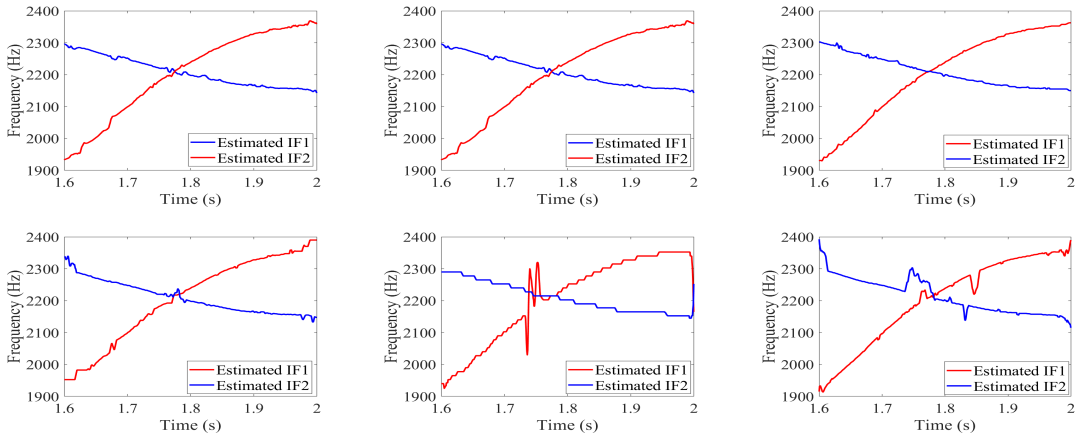


Figure 16: IF extraction results of SXWLCTs, TET and MESCT. First row (left to right): SXWLCT $n = 1$, SXWLCT $n = 5$, SXWLCT $n = 2$; Second row (left to right): SXWLCT $n = 6$, TET, MESCT (squeezing five times).

Overall, the WLCTs demonstrate substantial potential for signal separation in three-dimensional space, establishing a more versatile framework than the CT. The X-ray transform further enhances this framework by accelerating decay along the chirrate dimension, yielding a highly concentrated energy distribution. Whereas many existing synchrosqueezing techniques based on CT rely on specific reassignment operators, the proposed WLCT and XWLCT frameworks offer a more adaptable plat-

form for implementing and enhancing such operators. The results presented in this section confirm that integrating our framework with these advanced operators holds substantial promise and paves the way for more powerful time-frequency analysis tools.

6. Algorithm implementation

In implementing the discrete WLCTs, the core computational step involves constructing the discretized functions $\mathcal{L}^{M_{\lambda_l, n}}(g)(\lambda_l, \tau_k)$, while subsequent processing stages maintain close structural parallels with standard discrete WFT implementations.

Suppose the input signal $x(t)$ is discretized uniformly at points

$$t_m = t_0 + m\Delta t, \quad m = 0, 1, \dots, N - 1, \quad (55)$$

where Δt is the time-domain sample step, and N denotes the total number of sampling points. The chirprate variable λ is discretized into N_c bins, where N_c is the number of chirprate bins (one may set $N_c = 2 \lfloor \frac{N}{2} \rfloor$).

The values of λ are determined by the choice of n and the discretization method, as detailed below. For $n = 2, 6$, we adopt uniform sampling. First, we assume that the range of the variable λ is given by $-R_0 \leq \lambda \leq R_0$, where R_0 is a tunable parameter that can be adjusted based on the signal characteristics. Then, the discrete values of λ are defined as

$$\lambda_\ell = R_0 + (1 - \ell)\Delta\lambda, \quad \ell = 1, 2, \dots, N_c, \quad (56)$$

where the sampling interval $\Delta\lambda$ is given by

$$\Delta\lambda = 2R_0/(N_c - 1).$$

As for $n = 1$ or 5 , we define the discrete chirprates using a dyadic scaling structure. The positive chirprates are given by $\lambda_\ell^+ = a_0 \cdot 2^{j\Delta a}$, where a_0 is a fundamental scaling factor and Δa is a tunable resolution parameter. The corresponding negative chirprates are defined in a symmetric manner. The complete discrete chirprate set is then:

$$\lambda_\ell = \begin{cases} -a_0 \cdot 2^{(\lfloor N_c/2 \rfloor + 1 - \ell)\Delta a}, & \ell = 1, 2, \dots, \lfloor N_c/2 \rfloor \\ a_0 \cdot 2^{(\ell - \lfloor N_c/2 \rfloor - 1)\Delta a}, & \ell = \lfloor N_c/2 \rfloor + 2, \dots, N_c \end{cases} \quad (57)$$

where the scaling factor a_0 defaults to Δt but can be adapted to the signal characteristics.

Based on (11), substituting variables (56) or (57) into (11) allows us to obtain the discretized representations of $C_n(\lambda_\ell)$ and $P_n(\lambda_\ell)$, respectively. Here, C_n and P_n are defined in (12) with the

parameter matrix $M_{\lambda_l, n}$. Additionally, the time variable for the discrete window functions is defined as

$$\tau_k = (k - \lfloor \frac{N}{2} \rfloor) \Delta t, \quad k = 1, 2, \dots, N, \quad (58)$$

where Δt is the time step size. Thus, we can obtain the discrete representation of $\mathcal{L}^{M_{\lambda_l, n}}(g)(\lambda_\ell, \tau_k)$ as

$$\mathcal{L}^{M_{\lambda_l, n}}(g)(\lambda_\ell, \tau_k) = C_n(\lambda_\ell) e^{-P_n(\lambda_\ell)\tau_k^2}. \quad (59)$$

In fact, for the function $\tau^d \mathcal{L}^{M_{\lambda_l, n}}(g)(\tau)$ where $d = 1, 2$, we can discretize it as

$$\tau_k^d \mathcal{L}^{M_{\lambda_l, n}}(g)(\lambda_\ell, \tau_k) = \tau_k^d C_n(\lambda_\ell) e^{-P_n(\lambda_\ell)(\tau_k)^2}. \quad (60)$$

When dealing with the discretization of the frequency variable η , we have

$$\eta_j := \begin{cases} j\Delta\eta, & \text{for } 0 \leq j \leq \lfloor \frac{N}{2} \rfloor, \\ (j - N)\Delta\eta, & \text{for } \lfloor \frac{N}{2} \rfloor < j < N, \end{cases} \quad (61)$$

where $\Delta\eta := \frac{1}{N\Delta t}$. For the case when $0 \leq j \leq \lfloor \frac{N}{2} \rfloor$, the product $\eta_j \tau_k$ can be expressed as

$$\eta_j \tau_k = (k - \lfloor \frac{N}{2} \rfloor) \Delta t \cdot j \Delta\eta = \frac{(k - \lfloor \frac{N}{2} \rfloor) j}{N}.$$

We define the discrete transform $T_x^{g, n}(\lambda_l, \eta_j, t_m)$ as follows:

$$\begin{aligned} T_x^{g, n}(\lambda_l, \eta_j, t_m) &= \sum_{k=1}^N x(t_m + \tau_k) \mathcal{L}^{M_{\lambda_l, n}}(g)(\lambda_\ell, \tau_k) e^{-2\pi i \eta_j \tau_k} \Delta t \\ &= \sum_{k=1}^N x(t_m + \tau_k) \mathcal{L}^{M_{\lambda_l, n}}(g)(\lambda_\ell, \tau_k) e^{-2\pi i \frac{(k - \lfloor \frac{N}{2} \rfloor) j}{N}} \Delta t. \end{aligned} \quad (62)$$

This transform can be efficiently implemented using the fast Fourier transform (FFT). The overall computational complexity is $O(N_c N \log N)$, comparable to that of the CT implementation. As WLCTs produce three-dimensional time-frequency-chirp rate representations, processing long signals poses significant challenges in terms of memory requirements and computational load. This can be mitigated by reducing the number of chirp rate bins and incorporating a hop size parameter (analogous to the method used in the windowed Fourier transform) to accelerate computation and reduce memory consumption.

Substituting (59) with (60), we obtain the discrete expression for $T_x^{\tau^d g, n}(\lambda_l, \eta_j, t_m)$,

$$T_x^{\tau^d g, n}(\lambda_l, \eta_j, t_m) = \sum_{k=1}^N x(t_m + \tau_k) \tau_k^d \mathcal{L}^{M_{\lambda_l, n}}(g)(\lambda_\ell, \tau_k) e^{-2\pi i \frac{(k - \lfloor \frac{N}{2} \rfloor) j}{N}} \Delta t. \quad (63)$$

Then, we can define the discrete IF reference function and the chirprate reference function as follows:

$$\Lambda_x^{g,n}(\lambda_l, \eta_j, t_m) = \operatorname{Re} \left(i P_n(\lambda_l) + \frac{(T_x^{g,n}(\lambda_l, \eta_j, t_m))^2}{2\pi i \left((T_x^{\tau g,n}(\lambda_l, \eta_j, t_m))^2 - T_x^{g,n}(\lambda_l, \eta_j, t_m) T_x^{\tau^2 g,n}(\lambda_l, \eta_j, t_m) \right)} \right), \quad (64)$$

$$\Omega_x^{g,n}(\lambda_l, \eta_j, t_m) = \eta_j - \operatorname{Re} \left(\frac{T_x^{g,n}(\lambda_l, \eta_j, t_m) T_f^{\tau g,n}(\lambda_l, \eta_j, t_m)}{2\pi i \left((T_x^{\tau g,n}(\lambda_l, \eta_j, t_m))^2 - T_x^{g,n}(\lambda_l, \eta_j, t_m) T_x^{\tau^2 g,n}(\lambda_l, \eta_j, t_m) \right)} \right). \quad (65)$$

Finally, we summarize the above steps in Algorithm 1.

Algorithm 1 Implementation Procedure for WLCT and Calculations of Reassignment Operators

- 1: **Input:** $x(t_m)$, n , R_0 , N_c , a_0 , Δa , N
- 2: Discretize the chirprate λ_l using (56) or (57) based on n .
- 3: Discretize the frequency η_j and window time τ_k using (61) and (58).
- 4: **for** $l \leftarrow 1$ to N_c **do**
- 5: Precompute the discrete windows: $\mathcal{L}^{M_{\lambda_l,n}}(g)(\lambda_l, \tau_k)$, $\tau_k \mathcal{L}^{M_{\lambda_l,n}}(g)(\lambda_l, \tau_k)$, and $\tau_k^2 \mathcal{L}^{M_{\lambda_l,n}}(g)(\lambda_l, \tau_k)$, based on (59) and (60).
- 6: **for** $m \leftarrow 1$ to N **do**
- 7: Compute $T_x^{g,n}(\lambda_l, \eta_j, t_m)$ via FFT (see (62)).
- 8: Compute $T_x^{\tau g,n}(\lambda_l, \eta_j, t_m)$ and $T_x^{\tau^2 g,n}(\lambda_l, \eta_j, t_m)$ via FFT (see (63)).
- 9: Calculate the reassignment operators $\Lambda_x^{g,n}(\lambda_l, \eta_j, t_m)$ and $\Omega_x^{g,n}(\lambda_l, \eta_j, t_m)$ using (64) and (65).
- 10: **end for**
- 11: **end for**
- 12: **Output:**
- 13: The WLCT coefficients $T_x^{g,n}(\lambda_l, \eta_j, t_m)$
- 14: The reassignment operators: $\Lambda_x^{g,n}(\lambda_l, \eta_j, t_m)$ and $\Omega_x^{g,n}(\lambda_l, \eta_j, t_m)$

Besides, for multicomponent signals whose instantaneous chirprates are all positive (e.g., signal $y(t)$ in (45) and $z(t)$ in (54)), the computational complexity can be reduced by restricting the analysis to the positive chirprate domain. This can be achieved by redefining the chirprate grid with a bin size of $\lfloor \frac{N_c}{2} \rfloor$. Specifically, the chirprate discretization in (56) is replaced with

$$\lambda_\ell = -\ell \Delta \lambda, \quad \ell = 1, \dots, \left\lfloor \frac{N_c}{2} \right\rfloor,$$

while the discretization in (57) becomes

$$\lambda_\ell = a_0 2^{\ell \Delta a}, \quad \ell = 1, 2, \dots, \left\lfloor \frac{N_c}{2} \right\rfloor.$$

For signal $x(t)$ (given by (2)) with signal length $N = 512$, chirprate bin size $N_c = 513$, and frequency bin size $N_\eta = 256$, the required memory is approximately 1.0 GB. In contrast, for signal

$z(t)$ (given by (54)) with $N = 1024$, $N_\eta = 512$, and $N_c = 512$, the memory requirement is about 4.0 GB. Then, the corresponding runtimes for implementing the Algorithm 1 are provided in Table 3, respectively, measured on a standard laptop (Intel Core(TM) i7-14650HX CPU @ 2.20 GHz with 16 GB RAM).

Table 3: Runtime (in seconds) of Algorithm 1 for signals $x(t)$ and $z(t)$ with different n

Signal	$n = 1$	$n = 2$	$n = 5$	$n = 6$
$x(t)$	62.02	56.67	66.22	64.08
$z(t)$	210.70	199.67	203.80	216.88

Following this, we consider the reassignment algorithm. To further enhance the precision of the signal frequency and chirprate estimation, the frequency step size can be reset to $\Delta\xi$ and the chirprate step size to $\Delta\gamma$.

$$\begin{aligned}\gamma_p &= -R_0 + (p-1)\Delta\gamma, \quad p = 1, 2, \dots, N_1, \\ \xi_q &= (q-1)\Delta\xi, \quad q = 1, 2, \dots, N_2,\end{aligned}$$

where

$$N_1 = \frac{2R_0}{\Delta\gamma} + 1, \quad N_2 = \left\lfloor \frac{N}{2} \right\rfloor \frac{\Delta\eta}{\Delta\xi}.$$

Generally, $\Delta\gamma$ and $\Delta\xi$ are smaller than $\Delta\lambda$ and $\Delta\eta$. Therefore, the estimated ridges are more precise when this resetting is applied.

Then, we obtain

$$S_x^n(\gamma_p, \xi_q, t_m) = \sum_{(j, \ell) \in O_{p, q, m}} T_x^{g, n}(\lambda_\ell, \eta_j, t_m), \quad (66)$$

where the set $O_{p, q, m}$ is defined as

$$O_{p, q, m} := \left\{ (j, \ell) : \begin{array}{l} |\Lambda_x^{g, n}(\lambda_\ell, \eta_j, t_m) - \gamma_p| \leq \frac{1}{2}\Delta\gamma, \quad |\Omega_x^{g, n}(\lambda_\ell, \eta_j, t_m) - \xi_q| \leq \frac{1}{2}\Delta\xi, \\ |T_x^{g, n}(\lambda_\ell, \eta_j, t_m)| > \epsilon, \\ \left| (T_x^{\tau g, n}(\lambda_\ell, \eta_j, t_m))^2 - T_x^{g, n}(\lambda_\ell, \eta_j, t_m) T_x^{\tau^2 g, n}(\lambda_\ell, \eta_j, t_m) \right| > \epsilon \end{array} \right\},$$

with ϵ being a predefined threshold value.

Afterwards, we consider the implementation of the XWLCTs as described in Definition 4. We find it is quite flexible for the choice of $h(v)$. In this paper, we define

$$h(v_p) = \frac{1}{\sqrt{2\pi}} e^{-\frac{v_p^2}{2}}, \quad (67)$$

where the discrete points v_p are given by:

$$v_p = (p - N_0) \cdot \Delta v, \quad \text{for } p = 1, 2, \dots, 2N_0 + 1.$$

Here, Δv denotes the discretization step size for the window function, with a default value of $\Delta v = 2\Delta t$, and N_0 is set to 64 by default.

The X-ray transform is given by

$$\mathcal{T}_x^{g,n}(\lambda_l, \eta_j, t_m) = \sum_p |T_x^{g,n}(\lambda_l, \eta_j + \Lambda_l v_p, t_m + v_p)| h(v_p) \Delta v, \quad (68)$$

where

$$\Lambda_l = \begin{cases} -\lambda_l, & \text{for } n = 2 \text{ and } 6, \\ \frac{1}{\lambda_l}, & \text{for } n = 1 \text{ and } 5. \end{cases}$$

The detailed implementation steps are presented in Algorithm 2.

Algorithm 2 Implementation Procedure for XWLCT

```

1: Input: Discrete time points  $t_m$ ;  $n$ ,  $\Lambda_l$ ;  $\Delta v$ ,  $N_0$ ,  $\eta_j$ ,  $\Delta t, \Delta \eta$ ,  $N$ ,  $N_c$ ,  $N_f$ .
2: Construct the discrete window function  $h(v_p)$  according to (67).
3: for  $l \leftarrow 1$  to  $N_c$  do
4:   for  $m \leftarrow 1$  to  $N$  do
5:     for  $j \leftarrow 1$  to  $N_f$  do
6:       for  $p \leftarrow 1$  to  $2N_0 + 1$  do
7:         if  $0 < \eta_j + \Lambda_l v_p < N_f \Delta \eta$  and  $0 < t_m + v_p < N \Delta t$  then
8:            $\mathcal{T}_x^{g,n}(\lambda_l, \eta_j, t_m) = \mathcal{T}_x^{g,n}(\lambda_l, \eta_j, t_m) + |T_x^{g,n}(\lambda_l, \eta_j + \Lambda_l v_p, t_m + v_p)| h(v_p) \Delta v.$ 
9:         end if
10:        end for
11:      end for
12:    end for
13:  end for
14: Output: The XWLCT coefficients  $\mathcal{T}_x^{g,n}(\lambda_l, \eta_j, t_m)$ .

```

For the SXWLCTs $\mathcal{S}_x^n(\gamma_p, \xi_q, t_m)$, simply replace $T_x^{g,n}(\lambda_l, \eta_j, t_m)$ in (66) with $\mathcal{T}_x^{g,n}(\lambda_l, \eta_j, t_m)$ to obtain the desired modification. A time-frequency-chirprate representation with concentrated energy is obtained after applying the synchrosqueezed transform. The codes are available at:

<https://github.com/Lishuixin065/SXWLCT>.

7. Conclusion

In this paper, we introduce a novel windowed linear canonical transform (WLCT) to address multicomponent signals with overlapping instantaneous frequency (IF) curves. By employing the WLCT, we extend the traditional two-dimensional time-frequency plane into a three-dimensional framework, thereby offering richer representations for signal analysis. Our analysis and numerical experiments demonstrate that this approach holds significant potential for three-dimensional signal separation, effectively distinguishing and handling complex signal components. Furthermore, through the application of the X-ray transform and the synchrosqueezed transform, we achieve a more precise time-frequency-chirprate representation, providing accurate IF and chirprate estimations. These advancements further enhance the precision and methodology of signal processing.

Acknowledgments

This work was partially supported by the National Key Research and Development Program of China under Grants 2022YFA1005703 and the National Natural Science Foundation of China under Grants U21A20455 and 12571109.

References

- [1] M. Dakovic, L. Stankovic, T. Thayaparan, Time-Frequency Signal Analysis with Applications, Artech House, 2013.
- [2] I. Daubechies, Ten Lectures on Wavelets, SIAM, 1992.
- [3] S. Mallat, A Wavelet Tour of Signal Processing, Elsevier, 1999.
- [4] L. Cohen, Time-frequency Analysis, volume 778, Prentice Hall PTR New Jersey, 1995.
- [5] I. Daubechies, J. Lu, H.-T. Wu, Synchrosqueezed wavelet transforms: An empirical mode decomposition-like tool, *Applied and Computational Harmonic Analysis* 30 (2011) 243–261.
- [6] F. Auger, P. Flandrin, Improving the readability of time-frequency and time-scale representations by the reassignment method, *IEEE Transactions on Signal Processing* 43 (1995) 1068–1089.
- [7] T. Oberlin, S. Meignen, V. Perrier, Second-order synchrosqueezing transform or invertible reassignment? Towards ideal time-frequency representations, *IEEE Transactions on Signal Processing* 63 (2015) 1335–1344.

- [8] T. Oberlin, S. Meignen, The second-order wavelet synchrosqueezing transform, in: 2017 IEEE International Conference on Acoustics, Speech and Signal Processing (ICASSP), IEEE, 2017, pp. 3994–3998.
- [9] R. Behera, S. Meignen, T. Oberlin, Theoretical analysis of the second-order synchrosqueezing transform, *Applied and Computational Harmonic Analysis* 45 (2018) 379–404.
- [10] D.-H. Pham, S. Meignen, High-order synchrosqueezing transform for multicomponent signals analysis—With an application to gravitational-wave signal, *IEEE Transactions on Signal Processing* 65 (2017) 3168–3178.
- [11] G. Yu, M. Yu, C. Xu, Synchroextracting transform, *IEEE Transactions on Industrial Electronics* 64 (2017) 8042–8054.
- [12] G. Yu, Z. Wang, P. Zhao, Multisynchrosqueezing transform, *IEEE Transactions on Industrial Electronics* 66 (2018) 5441–5455.
- [13] S. Wang, X. Chen, G. Cai, B. Chen, X. Li, Z. He, Matching demodulation transform and synchrosqueezing in time-frequency analysis, *IEEE Transactions on Signal Processing* 62 (2013) 69–84.
- [14] S. Meignen, D.-H. Pham, S. McLaughlin, On demodulation, ridge detection, and synchrosqueezing for multicomponent signals, *IEEE Transactions on Signal Processing* 65 (2017) 2093–2103.
- [15] Q. Jiang, B. W. Suter, Instantaneous frequency estimation based on synchrosqueezing wavelet transform, *Signal Processing* 138 (2017) 167–181.
- [16] Q. Jiang, A. Prater-Bennette, B. W. Suter, A. Zeyani, Instantaneous frequency-embedded synchrosqueezing transform for signal separation, *Frontiers in Applied Mathematics and Statistics* 8 (2022) 830530.
- [17] D. He, H. Cao, S. Wang, X. Chen, Time-reassigned synchrosqueezing transform: The algorithm and its applications in mechanical signal processing, *Mechanical Systems and Signal Processing* 117 (2019) 255–279.
- [18] W. Li, Z. Zhang, F. Auger, X. Zhu, Theoretical analysis of time-reassigned synchrosqueezing wavelet transform, *Applied Mathematics Letters* 132 (2022) 108141.
- [19] J. Liu, Z. Meng, D. Sun, Y. Guan, W. Cao, J. Li, Local time-reassigned synchrosqueezing transform and its application in bearing fault characteristic extraction, *Mechanical Systems and Signal Processing* 203 (2023) 110726.

[20] D. Fourer, F. Auger, Second-order time-reassigned synchrosqueezing transform: Application to draupner wave analysis, in: 2019 27th European Signal Processing Conference (EUSIPCO), IEEE, 2019, pp. 1–5.

[21] Z. He, X. Tu, W. Bao, Y. Hu, F. Li, Gaussian-modulated linear group delay model: Application to second-order time-reassigned synchrosqueezing transform, *Signal Processing* 167 (2020) 107275.

[22] S. Mann, S. Haykin, The chirplet transform: Physical considerations, *IEEE Transactions on Signal Processing* 43 (1995) 2745–2761.

[23] L. Li, N. Han, Q. Jiang, C. K. Chui, A chirplet transform-based mode retrieval method for multicomponent signals with crossover instantaneous frequencies, *Digital Signal Processing* 120 (2022) 103262.

[24] C. K. Chui, Q. Jiang, L. Li, J. Lu, Analysis of a direct separation method based on adaptive chirplet transform for signals with crossover instantaneous frequencies, *Applied and Computational Harmonic Analysis* 62 (2023) 24–40.

[25] C. K. Chui, Q. Jiang, L. Li, J. Lu, Time-scale-chirp_rate operator for recovery of non-stationary signal components with crossover instantaneous frequency curves, *Applied and Computational Harmonic Analysis* 54 (2021) 323–344.

[26] V. Namias, The fractional order Fourier transform and its application to quantum mechanics, *IMA Journal of Applied Mathematics* 25 (1980) 241–265.

[27] L. B. Almeida, The fractional Fourier transform and time-frequency representations, *IEEE Transactions on Signal Processing* 42 (1994) 3084–3091.

[28] R. Tao, B. Deng, Y. Wang, *Fractional Fourier Transform and Its Applications*, Beijing: Tsinghua University Press, 2009.

[29] M. Moshinsky, C. Quesne, Linear canonical transformations and their unitary representations, *Journal of Mathematical Physics* 12 (1971) 1772–1780.

[30] S. A. Collins Jr, Lens-system diffraction integral written in terms of matrix optics, *Journal of the Optical Society of America* 60 (1970) 1168–1177.

[31] K.-I. Kou, R. Xu, Windowed linear canonical transform and its applications, *Signal Processing* 92 (2012) 179–188.

- [32] D. Wei, H. Hu, Theory and applications of short-time linear canonical transform, *Digital Signal Processing* 118 (2021) 103239.
- [33] D. Wei, Y. Li, Generalized wavelet transform based on the convolution operator in the linear canonical transform domain, *Optik* 125 (2014) 4491–4496.
- [34] Y. Guo, B. Li, The linear canonical wavelet transform on some function spaces, *International Journal of Wavelets, Multiresolution and Information Processing* 16 (2018) 1850010.
- [35] D. Wei, Y. Zhang, Y. Li, Linear canonical Stockwell transform: theory and applications, *IEEE Transactions on Signal Processing* 70 (2022) 1333–1347.
- [36] F. A. Shah, A. Y. Tantary, Linear canonical Stockwell transform, *Journal of Mathematical Analysis and Applications* 484 (2020) 123673.
- [37] R. Bai, B. Li, Q. Cheng, Wigner-Ville distribution associated with the linear canonical transform, *Journal of Applied Mathematics* 2012 (2012) 740161.
- [38] H. Xin, B. Li, On a new Wigner-Ville distribution associated with linear canonical transform, *EURASIP Journal on Advances in Signal Processing* 2021 (2021) 56.
- [39] Z. Zhao, B. Li, The spectrogram associated with the linear canonical transform, in: *Proceedings 2013 International Conference on Mechatronic Sciences, Electric Engineering and Computer (MEC)*, IEEE, 2013, pp. 1242–1245.
- [40] C. K. Chui, H. Mhaskar, Signal decomposition and analysis via extraction of frequencies, *Applied and Computational Harmonic Analysis* 40 (2016) 97–136.
- [41] C. K. Chui, Q. Jiang, L. Li, J. Lu, Signal separation based on adaptive continuous wavelet-like transform and analysis, *Applied and Computational Harmonic Analysis* 53 (2021) 151–179.
- [42] C. K. Chui, Q. Jiang, L. Li, J. Lu, Analysis of an adaptive short-time Fourier transform-based multicomponent signal separation method derived from linear chirp local approximation, *Journal of Computational and Applied Mathematics* 396 (2021) 113607.
- [43] X. Zhu, H. Yang, Z. Zhang, J. Gao, N. Liu, Frequency-chirprate reassignment, *Digital Signal Processing* 104 (2020) 102783.
- [44] Z. Chen, H.-T. Wu, Disentangling modes with crossover instantaneous frequencies by synchrosqueezed chirplet transforms, from theory to application, *Applied and Computational Harmonic Analysis* 62 (2023) 84–122.

[45] X. Zhu, Z. Zhang, J. Gao, Three-dimension extracting transform, *Signal Processing* 179 (2021) 107830.

[46] T. Chen, L. Xie, M. Cui, H. Su, Multiple enhanced synchrosqueezing in the time–frequency–chirprate space, *Signal Processing* 222 (2024) 109541.

[47] X. Chen, Z. Zhang, W. Yang, Composite signal detection using multisynchrosqueezing wavelet transform, *Digital Signal Processing* 149 (2024) 104482.

[48] K. Wolf, *Integral Transforms in Science and Engineering*, volume 11, Springer Science & Business Media, 2013.

[49] J. J. Healy, M. A. Kutay, H. M. Ozaktas, J. T. Sheridan, *Linear Canonical Transforms: Theory and Applications*, volume 198, Springer, 2015.

[50] S.-C. Pei, S.-G. Huang, Adaptive STFT with chirp-modulated Gaussian window, in: 2018 IEEE International Conference on Acoustics, Speech and Signal Processing (ICASSP), IEEE, 2018, pp. 4354–4358.

[51] B. Li, Z. Zhang, X. Zhu, Multitaper adaptive short-time Fourier transform with chirp-modulated Gaussian window and multitaper extracting transform, *Digital Signal Processing* 126 (2022) 103472.

[52] H. Bateman, B. M. Project, *Tables of Integral Transforms*, McGraw-Hill Book Company, 1954.

[53] L. Stanković, A measure of some time–frequency distributions concentration, *Signal Processing* 81 (2001) 621–631.

[54] Y.-L. Sheu, L.-Y. Hsu, P.-T. Chou, H.-T. Wu, Entropy-based time-varying window width selection for nonlinear-type time–frequency analysis, *International Journal of Data Science and Analytics* 3 (2017) 231–245.

[55] R. Zhang, Z. Wang, Y. Tan, X. Yang, S. Yang, Local maximum frequency-chirp-rate synchrosqueezed chirplet transform, *Digital Signal Processing* 130 (2022) 103710.

[56] G. H. Golub, C. F. Van Loan, *Matrix Computations*, JHU press, 2013.

[57] Q. Jiang, S. Li, J. Chen, L. Li, Synchrosqueezed X-ray wavelet–chirplet transform for accurate chirp rate estimation and retrieval of modes from multicomponent signals with crossover instantaneous frequencies, *Mechanical Systems and Signal Processing* 238 (2025) 113193.

- [58] A. Averbuch, Y. Shkolnisky, 3D discrete X-ray transform, *Applied and Computational Harmonic Analysis* 17 (2004) 259–276.
- [59] P. J. Miller, A. Shapiro, P. L. Tyack, A. Solow, Call-type matching in vocal exchanges of free-ranging resident killer whales, *orcinus orca*, *Animal Behaviour* 67 (2004) 1099–1107.